The Astrophysical Journal, 595:1277–1295, 2003 October 1

PHOTOSPHERIC MAGNETIC FIELD PROPERTIES OF FLARING VERSUS FLARE-QUIET ACTIVE REGIONS. I. DATA, GENERAL APPROACH, AND SAMPLE RESULTS

K. D. Leka and G. Barnes
Colorado Research Associates Division, NorthWest Research Associates, Inc., 3380 Mitchell Lane, Boulder, CO 80301;
leka@cora.nwra.com, graham@cora.nwra.com
Received 2003 March 1; accepted 2003 June 16

ABSTRACT

Photospheric vector magnetic field data from the University of Hawai'i Imaging Vector Magnetograph, with good spatial and temporal sampling, are used to study the question of identifying a preflare signature unique to flare events in parameters derived from the magnetic vector field, $\boldsymbol{B}$. In this first of a series of papers, we present the data analysis procedure and sample results focusing only on three active regions (NOAA Active Regions 8636, 8771, and 0030), three flares (two M class and one X class), and (most importantly) a flare-quiet epoch in a comparable flare-producing region. Quantities such as the distribution of the field morphology, horizontal spatial gradients of the field, vertical current, current helicity, "twist" parameter α, and magnetic shear angles are parameterized using their moments and appropriate summations. The time series of the resulting parameterizations are examined one at a time for systematic differences in overall magnitude and evolution between the flare and flare-quiet examples. The variations expected due to atmospheric seeing changes are explicitly included. In this qualitative approach we find (1) no obvious flare-imminent signatures from the plain magnetic field vector and higher moments of its horizontal gradient or from most parameterizations of the vertical current density; (2) counterintuitive but distinct flare-quiet implications from the inclination angle and higher moments of the photospheric excess magnetic energy; (3) flare-specific or flare-productivity signatures, sometimes weak, from the lower moments of the field gradients, kurtosis of the vertical current density, magnetic twist, current helicity density, and magnetic shear angle. The strongest results are, however, that (4) in ensuring a flare-unique signature, numerous candidate parameters (considering both their variation and overall magnitude) are nullified on account of similar behavior in a flare-quiet region, and hence (5) considering parameters one at a time in this qualitative manner is inadequate. To address these limitations, a quantitative statistical approach is presented in Paper II by Leka & Barnes.

Subject headings: Sun: activity — Sun: flares — Sun: photosphere — techniques: polarimetric

1. INTRODUCTION

It is a stated goal of solar active region research to understand the energy storage and release mechanism of solar flares, primarily as a purely scientific inquiry into the underlying physics; the solar atmosphere provides a laboratory of magnetized plasma where conditions exist that are difficult to simulate in the laboratory or on the computer. When the underlying physics is understood, then it should be possible to identify when the solar atmosphere becomes unstable to flaring. This is tantamount to solar flare prediction. The truly predictive aspects are important for those space-environment consequences, such as proton events, whose time of flight is close to the speed of light, which prohibits the more straightforward "now-casting" approach. We examine the energy storage and release mechanism by exploiting the information available in photospheric vector magnetogram data, beyond the analysis that has been performed to date in both scope and method.

Active regions are, at their simplest, concentrations of magnetic flux with a long-lived, bipolar structure. In a simple configuration, the magnetic fields resemble a simple dipole and display minimal "twist" of the field vectors, which would indicate excess energy stored in the fields. At their most complicated, active regions are a tangled collage of sunspots in a range of evolutionary states, an almost chaotic scene that changes hourly with the appearance and disappearance of rapidly evolving, often fast-moving sunspots. The magnetic fields in regions with such complex magnetic morphologies are rarely consistent with those expected from the low-energy potential field and instead are qualitatively described as having "twist" and "shear" and can be quantified by (for example) the presence of significant field-aligned current systems.

A solar flare can be characterized by a sudden nonthermal energy release, observable as an impulsive emission event in hard X-rays, an impulsive rise in soft X-rays (SXRs), and the release of high-energy charged particles (Sawyer, Warwick, & Dennett 1986 and references therein; Nitta 1997); although eruptive events are further characterized by their accompanying chromospheric ejecta, we focus here on flare events as detected in SXRs, specifically noting the start times for the *GOES* SXR rise as listed in the NOAA Space Environment Center's Event listings (Solar Geophysical Data 1998–2002).[1]

It is well known that the frequency and intensity of solar flares correlate well with the size and complexity of the host active region (Sawyer et al. 1986; McIntosh 1990); flare productivity has also been associated with rapidly emerging new magnetic flux (see, e.g., Schmieder et al. 1994; Wang, Xu, & Zhang 1994b; Choudhary, Ambastha, & Ai 1998; Nitta et al. 1996) and an overall reconfiguration of the

[1] Solar Geophysical Data Reports 1998–2002, Solar Event Reports, Space Environment Center/National Oceanic and Atmospheric Administration, US Dept. of Commerce, Boulder, CO.

magnetic fields (see, e.g., Fontenla et al. 1995; Wang, Jiong, & Hongqi 1998). However, these are not perfect correlations: some regions flare significantly only during the course of simplifying their magnetic morphology, and not all regions with complicated magnetic morphologies will produce large flares (McIntosh 1990; Patty & Hagyard 1986).

In the simple stress-and-release view of solar flare production, the magnetic fields in the corona are stressed because of evolution in the photosphere. The generally accepted mechanism for tapping the energy stored in the stressed fields is through magnetic reconnection, which can rapidly convert magnetic into kinetic and thermal energies. While the details of energy storage and its subsequent release have yet to be fully understood, the energy to power solar flares must be stored in the magnetic field. Should that field have a nonpotential configuration with significant field-aligned currents, the active region can easily store the 10^{30}–10^{33} ergs appropriate for flares (see, e.g., Tanaka & Nakagawa 1973; Krall et al. 1982; Silva et al. 1996; Metcalf et al. 1995).

The scenario outlined above could provide three observables indicative of impending energetic events and their passage: (1) indicator(s) of stored energy adequate to power an upcoming flare, (2) an instability threshold to be approached and exceeded, and (3) an accompanying postevent relaxation of the same quantity(ies). We focus on the first two points of the simple stress-and-release picture, ignoring the third for the following reason: at the lower boundary provided by the photosphere, forcing may be a continual process. As such, while forcing drives the instability that triggers magnetic reconnection in the chromosphere and corona, the relaxations will themselves occur in these upper layers and may not be evident in the photosphere. In addition, we argue that on a temporal basis, any aftereffects of reconnection visible in the photosphere will quickly (within our temporal cadence) be overwhelmed by the continued forcing and evolution.

Thus, it is the condition of the photospheric layer and its instability to the flaring state that we are interested in here. This condition may, for example, be described by an observable, such as the deviation of the photospheric vector magnetic field from a potential state, and its evolution as related to solar flare events, as might be expected from the stress-and-release model. To date, however, results from studies looking for such behavior have been quite mixed (Hagyard, West, & Smith 1993; Ambastha, Hagyard, & West 1993; Schmieder et al. 1994; Wang et al. 1994a). Here we embark upon a systematic study of the state of the photospheric magnetic properties of active regions as related to solar flares.

2. OBSERVATIONAL DATA

2.1. *Turning Photons into Vector Magnetic Flux Map Sequences*

The data used in this study are from the Imaging Vector Magnetograph (IVM) at the University of Hawai'i Mees Solar Observatory at Haleakala (Mickey et al. 1996; LaBonte, Mickey, & Leka 1999). Briefly, the spar-mounted IVM has a symmetric design with near-normal reflections and a helium-filled telescope to minimize instrumental polarization and internal seeing, respectively. A four-frame polarization-modulation sequence is used (Mickey et al. 1996); the requisite mixed polarization states are sampled by means of a Fabry-Pérot etalon at 30 wavelength positions across the magnetically sensitive ($g_{\rm eff} = 2.5$) Fe I 630.25 nm spectral line.

The raw data sample an active region with 512^2 0$''$.55 pixels, which covers most active regions (see Fig. 1). Each polarization- and spectrally sampled data set is acquired in

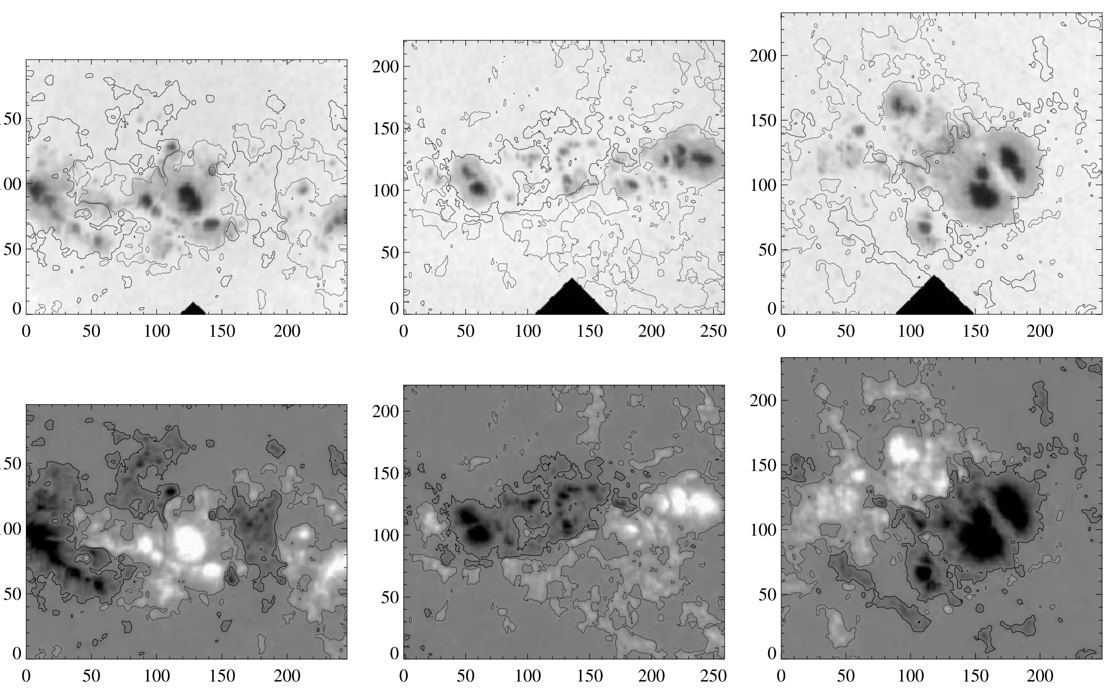

FIG. 1.—Images of continuum (*top*) and B_z (*bottom*, with ±100 G contours) of NOAA AR 0030 (*left*), AR 8636 (*middle*) and AR 8891 (*right*). Axes are approximately in megameters, and black triangles are masked-out field stops.

less than 2 minutes; for signal-to-noise ratio considerations, we combine pairs of raw data for a temporal cadence of approximately 4 minutes. Corrections to the raw data are performed to remove spatial and polarization distortions from both the telescope system and atmospheric seeing (Mickey et al. 1996; LaBonte et al. 1999). The data are then demodulated to produce Stokes spectra ($[I, Q, U, V]$) at each pixel (LaBonte et al. 1999). As a final step, the spectra are binned to 256^2 1\".1 pixels. The final polarization noise (normalized by the continuum intensity) is on the order of 2×10^{-3} in these data.

To derive the magnetic field vector from the resulting spectropolarimetric data, a forward-integration scheme based on the equations of Landolfi & Landi Degl'Innocenti (1982) and Landolfi, Landi Degl'Innocenti, & Arena (1984) is employed, which produces results comparable to a full least-squares inversion, with little evidence for systematic saturation or magneto-optical effects. We present here the magnetic flux density, i.e., the intrinsic field strength multiplied by the fill fraction, or the pixel-averaged flux density, with units of gauss (rather than Mx cm^{-2}) for simplicity. Furthermore, for lexical consistency, we refer to the vector magnetic field hereafter, even with the implicit fill-factor considerations. The resulting maps of the observed line-of-sight and transverse magnetic components have uncertainties on the order of 10 G (B_ℓ) and 25 G (B_t), with an uncertainty in the azimuthal angle of approximately 5°; in practice, the uncertainties are determined independently for each magnetogram.

The 180° ambiguity in the observed transverse component is resolved using an automated iterative procedure that first minimizes the difference between the observed field and a force-free field computed using the B_z component and a force-free twist parameter "α," itself chosen as that for which the resulting ambiguity resolution is least variable over the time series. This α was usually close to the best-fit force-free parameter "$\alpha_{\rm ff}$" discussed in § 3.2.5 and rarely differed by more than a factor of 2. After the initial comparison between observed and computed force-free fields, the automated procedure minimizes the field's divergence and the total vertical current (Canfield et al. 1993). Along with a spatial map of the resulting heliographic B_x, B_y, and B_z components, we derive corresponding maps of their uncertainties computed using the noise in the observed fields, the uncertainties returned from the inversion, and the coordinate transforms as described in Leka & Skumanich (1999).

The temporal sequence of vector magnetic field maps is then aligned on a subpixel grid for pointing variations and trimmed for edge data that are not present given the realignments. The final data cube consists of $[x, y, \boldsymbol{B}, t]$ and is stored in an easily accessible "structure" format of the IDL system for analysis.

3. ANALYSIS APPROACH AND RESULTS

We compare data for three active regions (see Fig. 1) and their temporal evolution with respect to one large and two moderate flare events and with respect to a flare-quiet epoch in an otherwise moderately flare-productive active region (see Table 1). All regions were large and forecast to flare by the NOAA Space Environment Center. Even though the regions were observed close to disk center, all projection effects are removed with the use of the full magnetic vector, and we work in the physically relevant heliographic coordinate system.

The quantities considered here were chosen on the following bases: (1) they contribute to the overall characterization of the physical state of the magnetic photosphere, and/or (2) they have been implemented by other researchers in the context of investigating solar activity.

The list of physical quantities examined is by no means exhaustive, although it is quite extensive (see below). Still, we limit this study to those quantities derivable from the IVM data and focus even further on a few examples chosen to illustrate potential successes and problems of this and previous studies. Beyond this, in Leka & Barnes (2003, hereafter Paper II) a full statistical approach is employed that demonstrates an approach to evaluating how useful each parameter is as a discriminant between a flare-imminent and a flare-quiet photosphere, using a larger sample of active regions and events.

3.1. *Accounting for Variations Due to Seeing*

For all ground-based time series observations, variations in the terrestrial atmosphere impart variations on resulting derived quantities. Relying solely on space-borne instruments is expensive, and in many cases the required instruments do not (yet) exist, as in the case of vector magnetic field observations. Hence, the seeing variations must be accounted for.

In this study the method described in Leka & Rangarajan (2001) is employed. In brief, for each time series, the magnetogram with the best seeing is used as a fiducial. The *raw* data (after only flat-fielding and dark-current correction) are artificially degraded with a range of Gaussian blur functions to mimic worsening (average) seeing conditions. The blurred raw data are fully reduced, demodulated, and analyzed in exactly the same manner as the "true" data, including trimming to match the time series data cube, computing the heliographic $\boldsymbol{B}$ vector, uncertainties, and parameters as described below. The range of blur used is such that the resulting degraded magnetograms cover the range of seeing in the temporal sequence of "real" data; specifically, 5–7 widths of the Gaussian blur function are

TABLE 1
ACTIVE REGIONS AND EVENTS

NOAA AR No.	Date	IVM Data UT range	Mag. Class	McIntosh Class	Area (μH)	Location	Event Time	SXR Class
8636	1999 Jul 23	16:47–18:50	$\beta\gamma\delta$	Fki	550	N19 E02	18:32	M1.1 ERU
8891	2000 Mar 01	19:43–21:24	$\beta\gamma$	Eki	1030	S16 E05	...	...
0030	2002 Jul 15	18:53–21:06	$\beta\gamma\delta$	Fkc	780	N19 E02	19:59	X3.0
							21:03	M1.8

applied across a range from 0″.5 to 2″.0, depending on the range observed in the data.

The resulting parameters derived from the degraded magnetic flux maps are then used to model the degradation in each parameter as a function of seeing. This function is incorporated as an additional source of uncertainty. That is, while the data are not themselves modified per se, the expected variation due to the evaluated seeing for each magnetogram is given. The asymmetric nature of the uncertainty can be used to estimate what the magnitude of "corrected" data would be. As shown in Leka & Rangarajan (2001), the results vary significantly between parameters derived from the vector field and can also vary significantly between active regions.

Blurring by atmospheric seeing can mimic the effect of degraded spatial resolution (Leka 1999). As such, readers are cautioned that the magnitudes of quantities presented here are best compared to those from instruments of similar spatial, spectral, and temporal sampling.

3.2. *The Parameters*

The quantities available for analysis are those derivable from the distribution functions of continuum intensity and the vector magnetic flux. The spatial distributions of each derived quantity are parameterized such that a single number represents the state of that quantity at that time. That is, we avoid a detailed spatial examination of each magnetogram and instead parameterize the state of the magnetic photosphere. Thus, we engage the first four moments of each distribution:

$$\text{mean } \bar{x} = \frac{1}{n}\sum_i x_i \,, \tag{1}$$

$$\text{standard deviation } \sigma = \left[\frac{1}{n}\sum_i (x_i - \bar{x})^2\right]^{1/2} \,, \tag{2}$$

$$\text{skew } \varsigma = \frac{1}{n}\sum_i \left[\frac{x_i - \bar{x}}{\sigma}\right]^3 \,, \tag{3}$$

$$\text{kurtosis } \kappa = \frac{1}{n}\sum_i \left[\frac{x_i - \bar{x}}{\sigma}\right]^4 - 3.0 \,, \tag{4}$$

with uncertainties in these quantities derived from the uncertainties in the data. The mean and standard deviation are in common usage, essentially describing the average and width of the distribution. The third moment, skewness, describes the asymmetry of a distribution and is a signed quantity sensitive to a distribution's tail due to its third power. A Gaussian distribution has zero skew, while a large positive/negative skew results from a distribution with a large positive/negative tail. The kurtosis tends toward zero for a Gaussian distribution *because of the −3.0 normalization* and is nonzero for non-Gaussian distributions or those composed of disparate populations.

As an example, consider the distribution of normal magnetic flux and its change between two (not consecutive) magnetograms (Fig. 2, Table 2). It is apparent that the distributions have changed, especially in the far-positive wing. The mean increases slightly between the two magnetograms, although the standard deviation decreases, primarily

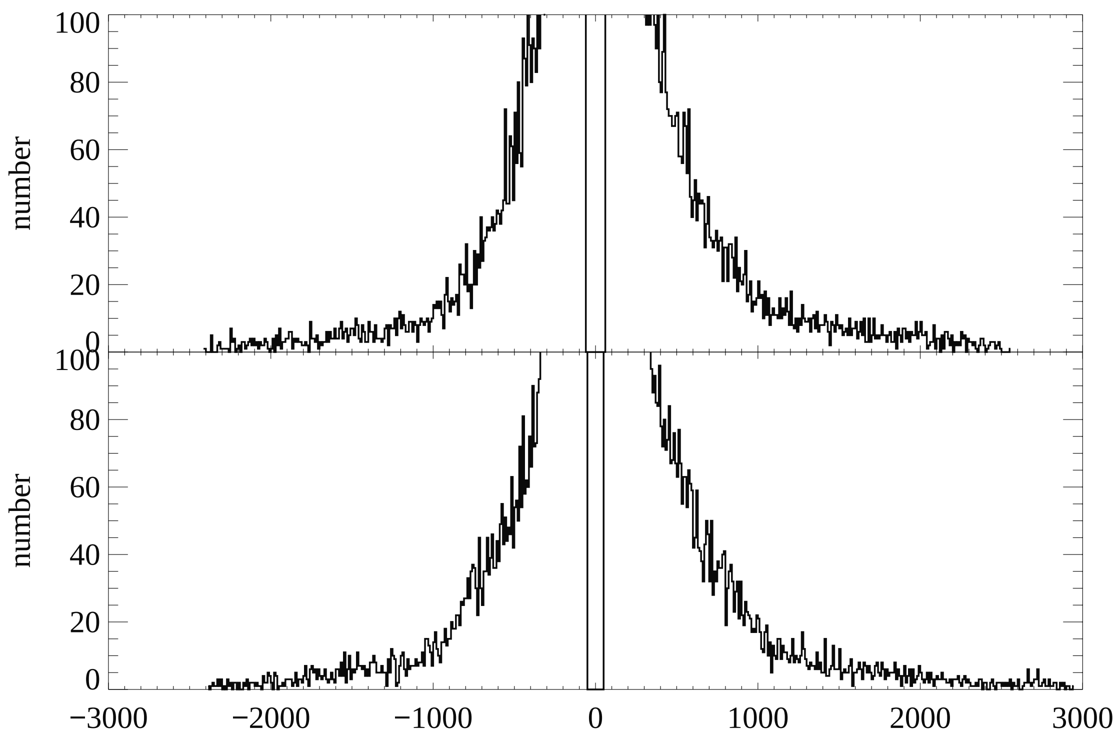

Fig. 2.—*Top*: Histogram of B_z for 20:58 UT magnetogram from AR 0030. The points below the 3 σ noise threshold are not included, and the data have been binned by a factor of 10. *Bottom*: Same as top plot for a magnetogram at 19:28 UT. See text for description of the statistical characterizations of these distributions.

TABLE 2
STATISTICAL CHARACTERIZATION AND PARAMETERIZATION OF NORMAL MAGNETIC FLUX DISTRIBUTION

UT Time	Mean	Standard Deviation	Skew	Kurtosis
20:58	41.2 ± 0.2	564.2 ± 0.2	0.307 ± 0.002	3.39 ± 0.01
19:28	44.2 ± 0.1	554.7 ± 0.1	0.552 ± 0.002	4.38 ± 0.01

because of a decrease in the central distribution width. The increase in both the skew and kurtosis are directly related to the extension of the positive wing. The power of using all four statistical descriptors is that both bulk and subtle changes are detectable through the use of the first two and higher order moments, respectively.

In some cases, an additional descriptor is used that either has physical significance or has been discussed in previous literature (e.g., the simple total of the quantity in question). In the example from above, the additional descriptors are the total (unsigned) and net (signed) magnetic flux over the field of view. For net quantities, we consider the absolute value of the computed signed quantity, with the thought that the quantity under consideration is simply the deviation from zero, irrespective of whether the net is positive or negative, which might be influenced by hemispheric or field-of-view biases.

In all cases, the quantities under consideration are computed only for those regions above 3 σ detections in either the quantity itself (e.g., the magnetic field components) or the "ingredient" parameters, (e.g., the horizontal magnetic field for J_z, since it is derived from the curl of the former). Thus, regions where derived quantities are well determined but small in magnitude are included, while conversely, regions where the same quantities are of large magnitude but are poorly determined are omitted.

In addition, in all cases we consider both the "background levels" or temporal mean of the quantity (e.g., the mean total magnetic flux) and its temporal variation (e.g., indicative of emerging/disappearing flux) for quantitative clues to activity level and/or impending events.

We compare the three flare events (in NOAA Active Regions 0030 and 8636) to a large and moderately complicated region (AR 8891) that was flare-productive on other days (Fig. 1). We strive to ensure that any changes seen are either repeatable between events *or* are uniquely associated with a flare event and not random. We focus on the few hours prior to an event, chosen primarily because of the timescale for significant evolution in active regions and the lead time required in true forecasting efforts for energetic events (Jones et al. 2002).

3.2.1. *Distribution of* $\boldsymbol{B}$

Numerous quantities are derived directly from the magnetic field vector. We consider the distributions of the spatially sampled [denoted by "s" rather than "(x, y)" for simplicity] $B_z(s)$, $B_h(s) = [B_x^2(s) + B_y^2(s)]^{1/2}$, and $B(s) = [B_x^2(s) + B_y^2(s) + B_z^2(s)]^{1/2}$, the latter two being positive-definite quantities. Following the example described above (and in Fig. 2 and Table 2), the distributions and their evolution are characterized by their four moments, beginning with B_z (Fig. 3).

We expect to be able to interpret flare-triggering magnetic field evolution using the temporal variations of the moments of the field distributions. Consider first the case of a symmetric (bipolar) sunspot pair emerging within an active region as a trigger for flares: its appearance will change the distribution of B_z so that the mean and skew would be unaffected, but the resulting even-order moments, standard deviation and kurtosis, would increase because of the appearance of strong-field "bumps" in both the positive and negative wings. If the scenario is modified so that not all of the emerging flux region is contained within the field of view, then the mean and skew would additionally change because of the flux imbalance, with the higher order moments being most sensitive to the changes in the distribution wings. One can additionally imagine that an imbalance in the concentration of the emerging magnetic fields, between leading and following polarities, for instance, would lead to more complicated interplays between changes in the mean, standard deviation, skew, and kurtosis. Thus, no single moment can be used to interpret the cause of its own variation; all four moments are required.

One can also characterize active regions by, for example, the overall levels of the moments and consider flare productivity in the context of thresholds. That is, one might determine that regions that display oppositely signed means and skews, for example, are generally flare-productive. While this analysis does not take advantage of the temporal sampling available in these data, it can lead to a more quantitative description of the flare-productive solar atmosphere.

Turning to the present data (see Fig. 3), the mean $\overline{B_z}$ is a signed quantity that reflects the overall polarity imbalance of the normal field within the observed field of view. As such, no physical significance should be attached to the fact that the flare-producing regions both have $\overline{B_z} > 0$, while AR 8891 has $\overline{B_z} < 0$. No significant change is visible for AR 0030 and AR 8636, although a small variation is observed for AR 8891, the flare-quiet region. The standard deviation $\sigma(B_z)$ is larger in magnitude for AR 8891 than in the flare-productive regions and decreases slightly with time. The three regions have quite different skews, with $\varsigma(B_z) > 0$ for AR 0030, $\varsigma(B_z) \approx 0$ for AR 8636, and $\varsigma(B_z) < 0$ for AR 8891. The skews for AR 0030 and AR 8891 indicate that there are significant positive and negative $\overline{B_z}$ tails, consistent with their respective $\overline{B_z}$ results. The kurtosis $\kappa(B_z)$ is similar for those two regions but larger for AR 8636, which itself had almost no skew. Hence, a picture emerges of two regions, one flare-productive and the other not, that otherwise have similar, fairly balanced distributions of the normal magnetic flux (AR 0030 and 8891) and tails of the flux distribution of opposite polarity. These contrast with the inferred $B_z(s)$ distribution of AR 8636, which is offset more to positive polarity, narrower, and more symmetric (less skew), but with larger non-Gaussian "bumps" on both wings (larger kurtosis).

The total magnetic flux is a quantitative measure of an active region's size, which is well correlated with its overall productivity for energetic events (Giovanelli 1939; McIntosh 1990; Canfield, Hudson, & McKenzie 1999; Tian, Liu, & Wang 2002a). Using the magnetic flux as a measure of size, rather than the white-light area, provides a more physical clue as to the energy available for such events. We consider here the total unsigned flux $\Phi_{\rm tot} = \sum |B_z| \, dA$, as well as the unsigned total flux for each polarity separately: $\Phi^+ = \sum B_z^+ \, dA$, $\Phi^- = \sum B_z^- \, dA$, where B_z^+, B_z^- are the

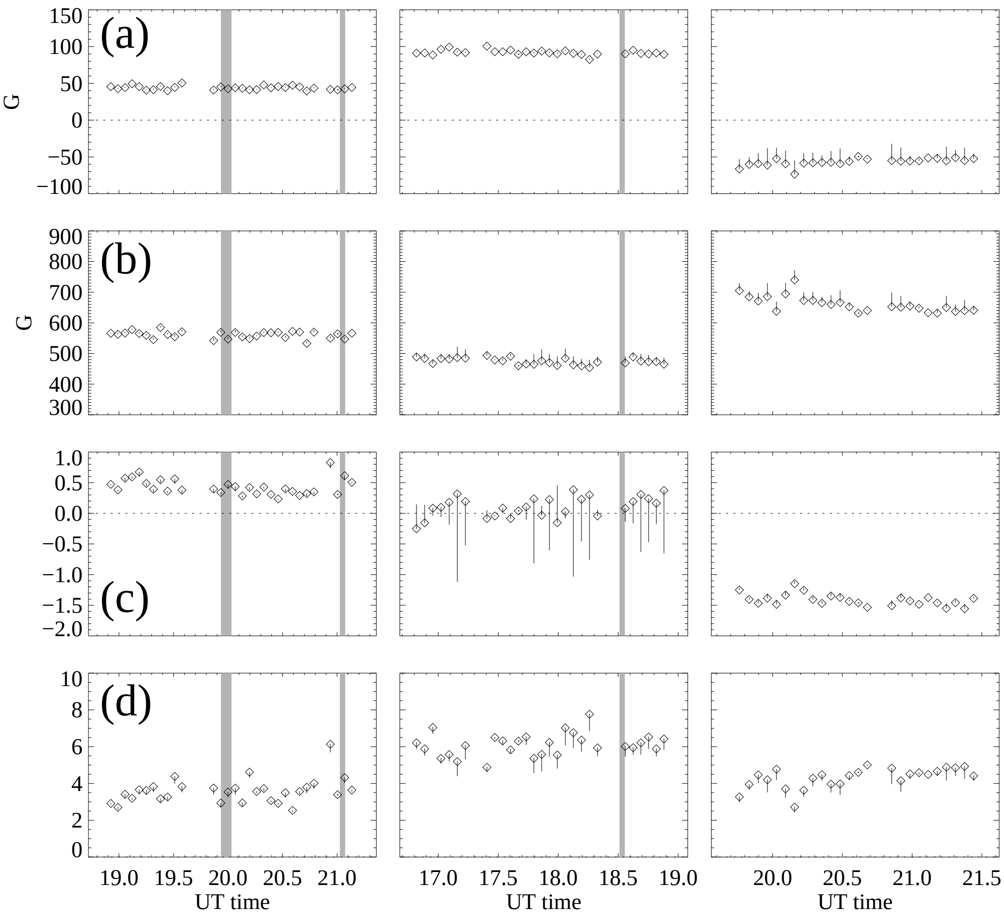

FIG. 3.—Examples of parameters discussed in the text for (*left to right*) AR 0030, AR 8636, and AR 8891. The start times of the flares as determined by the *GOES* SXR light curve are indicated by vertical gray lines, the X3.0 (*thick lines*) and M1.8 in AR 0030 and M1.1 ERU flares in AR 8636 (*thin lines*); AR 8891 did not produce any flares during this epoch. The x-axes indicate the UT time, y-axes are in the relevant units, and 1 σ error bars are plotted (for the 3 σ data), including the expected variation due to measured changes in the seeing conditions. Shown are the temporal variations of the four moments of the spatial distribution of the normal magnetic flux: (*a*) $\overline{B_z}$, (*b*) $\sigma(B_z)$, (*c*) $\varsigma(B_z)$, and (*d*) $\kappa(B_z)$.

positive- and negative-polarity vertical magnetic fields. The net flux imbalance in the field of view $|\Phi_{\rm net}| = |\sum B_z\, dA|$ is a quantity that has been associated with flare activity (Zhang et al. 1994; Tian et al. 2002a), although with little discussion as to the physical cause any (local) imbalance may have in flare productivity rather than the obvious field-of-view effects to which it is susceptible. Nevertheless, we consider this quantity but take its absolute value to avoid hemispheric biases imparted by the often asymmetric nature of the spatial flux distribution between preceding and following polarities.

Sample results for total and net flux are shown in Figure 4. The three regions considered are comparable in size [(4–6) $\times 10^{22}$ Mx], although the flare-quiet AR 8891 is the largest. None of the regions is flux-balanced, and AR 8636 is the farthest from balance by 10^{22} Mx; this is hardly a surprising result, given a restricted (even if large) field of view. Changes in the total and net magnetic flux have been associated with flare activity, both increasing (emerging) flux (Nitta et al. 1996; Choudhary et al. 1998; Ishii, Kurokawa, & Takeuchi 1998; Li et al. 2000a) and decreasing or disappearing flux (Wang et al. 2002a). Hence, the temporal evolution of these area-totaled quantities should document the general evolution of the overall magnetic flux content of the active region. Both flaring regions show small variations on the timescales shown here, with some flux growth in AR 8636. There is neither a visible "jump" in flux prior to the flare event nor a visible postevent decrease in flux. In addition, the changes are generally not beyond the uncertainties, especially when seeing is accounted for.

The horizontal component of the field has a distribution that is positive-definite and, as such, will indicate different things about the spatial structure of the magnetic field. The overall level of $\overline{B_h}$ is largest for AR 8891 (Fig. 5), which has the largest $\sigma(B_h)$ as well. The former shows some decrease prior to the three flares, indicating an evolution toward a more vertical field; this is not flare-specific, however, since there is a steady decrease in AR 8891 as well. The overall level of $\varsigma(B_h)$ is similar for all three regions: it is positive, indicating a contribution from a horizontal strong-field population, i.e., penumbral fields. The $\varsigma(B_h)$ and $\kappa(B_h)$ parameterizations are temporally quite variable for all three regions. By choosing temporal windows on a case-by-case basis, one can argue that they increase prior to the M-flare in AR 0030, decrease before the flare in AR 8636, and display a general increasing trend in AR 8891. It is unsatisfactory to state these trends as results, however,

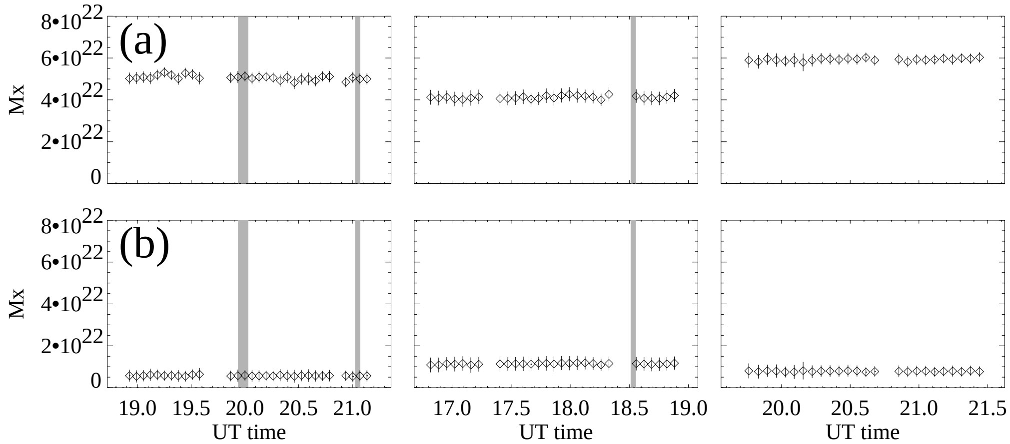

FIG. 4.—Same as Fig. 3, but for (*a*) the total unsigned magnetic flux $\Phi_{\rm tot}$ and (*b*) the absolute value of the net (signed) magnetic flux, $|\Phi_{\rm net}|$

because of the parameters' inconsistent behavior relative to the flare events and in the required " custom " temporal window over which the variations are observed.

In summary, using the distributions of the magnetic field vector for these examples, we find no obvious and consistent difference between the flare-productive and flare-quiet regions and no obvious and consistent evolution that occurs in the preflare periods.

3.2.2. *The Inclination Angle* γ

We consider the inclination angle as defined by

$$\gamma(s) = \tan^{-1}(|B_z|/B_h) , \quad (5)$$

defined such that fields approaching vertical return a small inclination angle, while fields approaching horizontal return inclination angles approaching 90°. The distribution of the

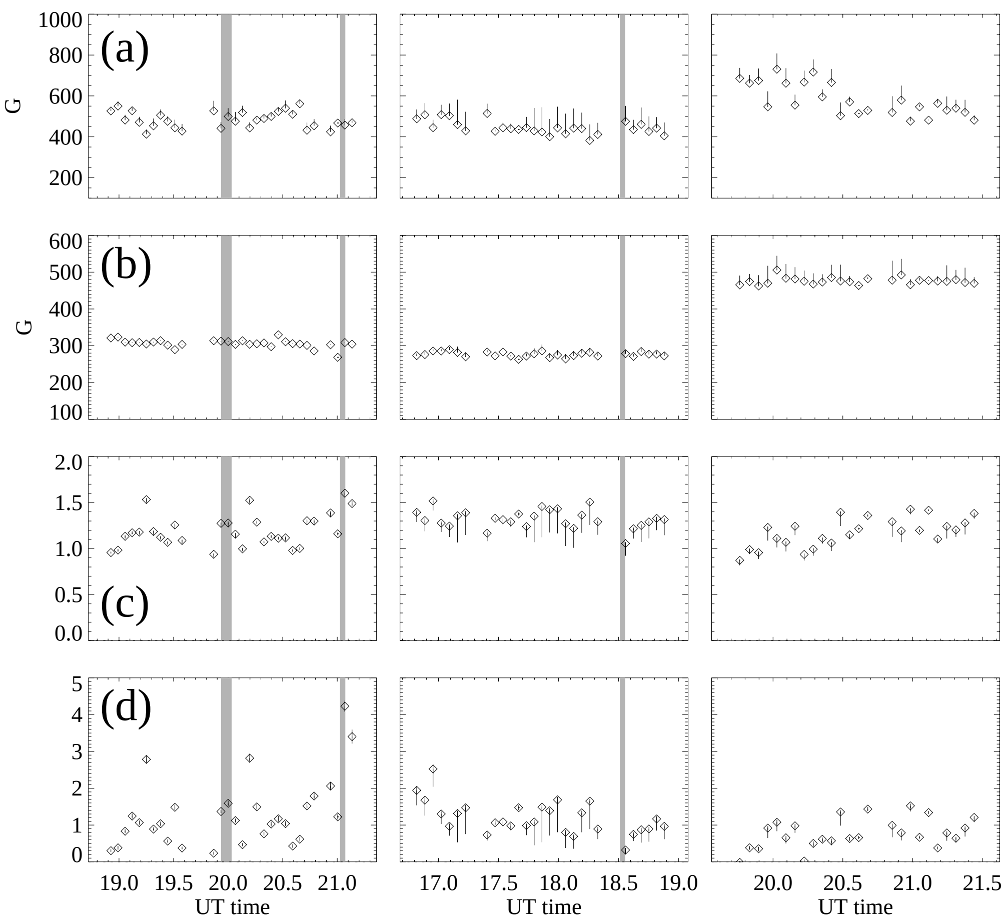

FIG. 5.—Same as Fig. 3, but for the four moments of the positive-definite distribution of the horizontal magnetic flux, (*a*) $\overline{B_h}$, (*b*) $\sigma(B_h)$, (*c*) $\varsigma(B_h)$, and (*d*) $\kappa(B_h)$.

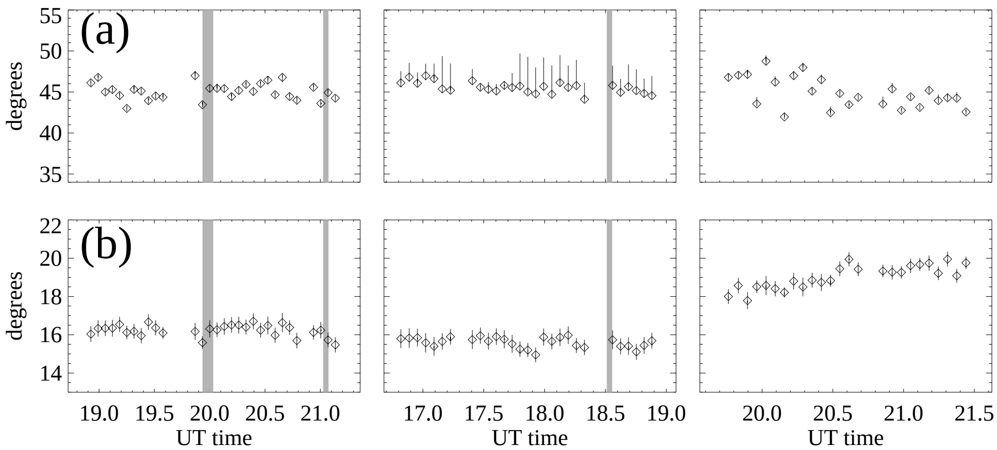

FIG. 6.—Same as Fig. 3, but for the first two moments of the distribution of the magnetic inclination angle, (*a*) $\bar{\gamma}$ and (*b*) $\sigma(\gamma)$

inclination angle over the region can detect the evolution of, for example, emerging flux regions as their magnetic morphology evolves from being primarily horizontal to primarily vertical. (N.B. The kurtosis is systematically negative because of the box car–type distribution and restricted range of the inclination angles; variations from this are difficult to determine, and hence we focus on the lower order moments).

All three regions (Fig. 6) have mean inclination angles of approximately 45°, indicating a mix of vertical (umbral, pore) and horizontal (penumbral, emerging) fields. Flare-quiet AR 8891 shows a long-term decreasing trend in $\bar{\gamma}$ (toward more vertical fields), where as neither AR 0030 nor AR 8636 show visible hours-long trends. Flare-quiet AR 8891 also has a larger and more variable $\sigma(\gamma)$, which could, in fact, be inferred from the larger $\sigma(B_z)$, $\sigma(B_h)$ levels for AR 8891 mentioned above. When a short time period (at most 30 minutes) prior to the flares is specified, one could argue that a slight decrease in $\sigma(\gamma)$ is detected. Again, similar short time periods in AR 8891 show decreases of comparable magnitudes, thus nullifying any necessary connection to preflare evolution.

From these few examples it appears that, counter-intuitively, an overall smaller $\sigma(\gamma)$ is present in the regions with higher immediate flare productivity; yet there is no unique preflare signature observed in the temporal variation of either $\bar{\gamma}$ or $\sigma(\gamma)$.

3.2.3. *Spatial Gradients of B, B_h, and B_z*

Spatial gradients of the magnetic field vector begin to quantify the complexity of the active region by specifying how "packed together" the concentrations of flux are; that is, the magnitude of the horizontal spatial gradients of the field quantifies the "sunspot distribution" component of the McIntosh classification (McIntosh 1990) and has generally been correlated with flare activity (McIntosh 1990; Zirin & Wang 1993; Zhang et al. 1994; Tian et al. 2002a; Gallagher, Moon, & Wang 2002). We consider here the magnitude of the horizontal spatial gradient of B:

$$|\nabla_h B(s)| = \left[\left(\frac{\partial B}{\partial x}\right)^2 + \left(\frac{\partial B}{\partial y}\right)^2\right]^{1/2} \qquad (6)$$

and similarly $|\nabla_h B_z(s)|$, $|\nabla_h B_h(s)|$. As per our standard approach, these distributions are parameterized using the four moments.

The behavior of $|\nabla_h B(s)|$, $|\nabla_h B_z(s)|$, and $|\nabla_h B_h(s)|$ is similar but not identical, according to the details of the field morphologies (Fig. 7). For example, $\overline{|\nabla_h B|}$, $\overline{|\nabla_h B_z|}$, and $\overline{|\nabla_h B_h|}$ all behave similarly, with subtle variations that depend on both the spatial gradients and the field strengths in the vertical and horizontal components. Hence, we show higher moments only of $|\nabla_h B_h(s)|$. Flare-quiet AR 8891 has the largest overall $\overline{|\nabla_h B_z|}$ level of the three, by a small amount. One could conclude from the examples presented here that as a flare-predictor threshold, neither $\overline{|\nabla_h B|}$ nor $\overline{|\nabla_h B_h|}$ perform particularly well. There appears to be a decrease in $\overline{|\nabla_h B|}$ and similarly in $\overline{|\nabla_h B_h|}$ for AR 8891, and neither AR 0030 nor AR 8636 shows similar hours-long trends. With a suitable choice of time windows, a preflare increase in $\overline{|\nabla_h B|}$ and $\overline{|\nabla_h B_z|}$ is visible, although the uncertainties due to seeing and the requirement of "custom" windows prohibits a more definitive statement. The $\varsigma(|\nabla_h B_h|)$ and $\kappa(|\nabla_h B_h|)$ both show changes in preflare epochs with similar custom time restrictions; similar variations occur in AR 8891 as well, hence negating these variations as unique preflare results.

Parameterizing the distribution of horizontal spatial gradients of the $\boldsymbol{B}$ components quantifies the "compactness" of the field distribution and its evolution. There is a small excess $\overline{|\nabla_h B_z|}$ in the flare-quiet region over the other two, counter to expectations. There is no objective and unique flare-specific signature from any moment of $|\nabla_h B_h(s)|$ [but cf. the examples using $\kappa(|\nabla_h B_h|)$ in Paper II].

3.2.4. *Vertical Current Density J_z*

The extent to which an active region stores energy above that supplied by the lowest energy configuration (e.g., a potential field) can be measured in numerous ways. We begin here simply with the curl of the $\boldsymbol{B}_h(s)$ vector as measured by the vertical current density:

$$J_z(s) = \frac{C}{\mu_0}\left(\frac{\partial B_y}{\partial x} - \frac{\partial B_x}{\partial y}\right), \qquad (7)$$

where μ_0 is the permeability of free space ($4\pi \times 10^{-7}$ H m^{-1}) and C contains constants related to unit conversion, giving J_z in mA m^{-2}; this quantity is computed at the intersection

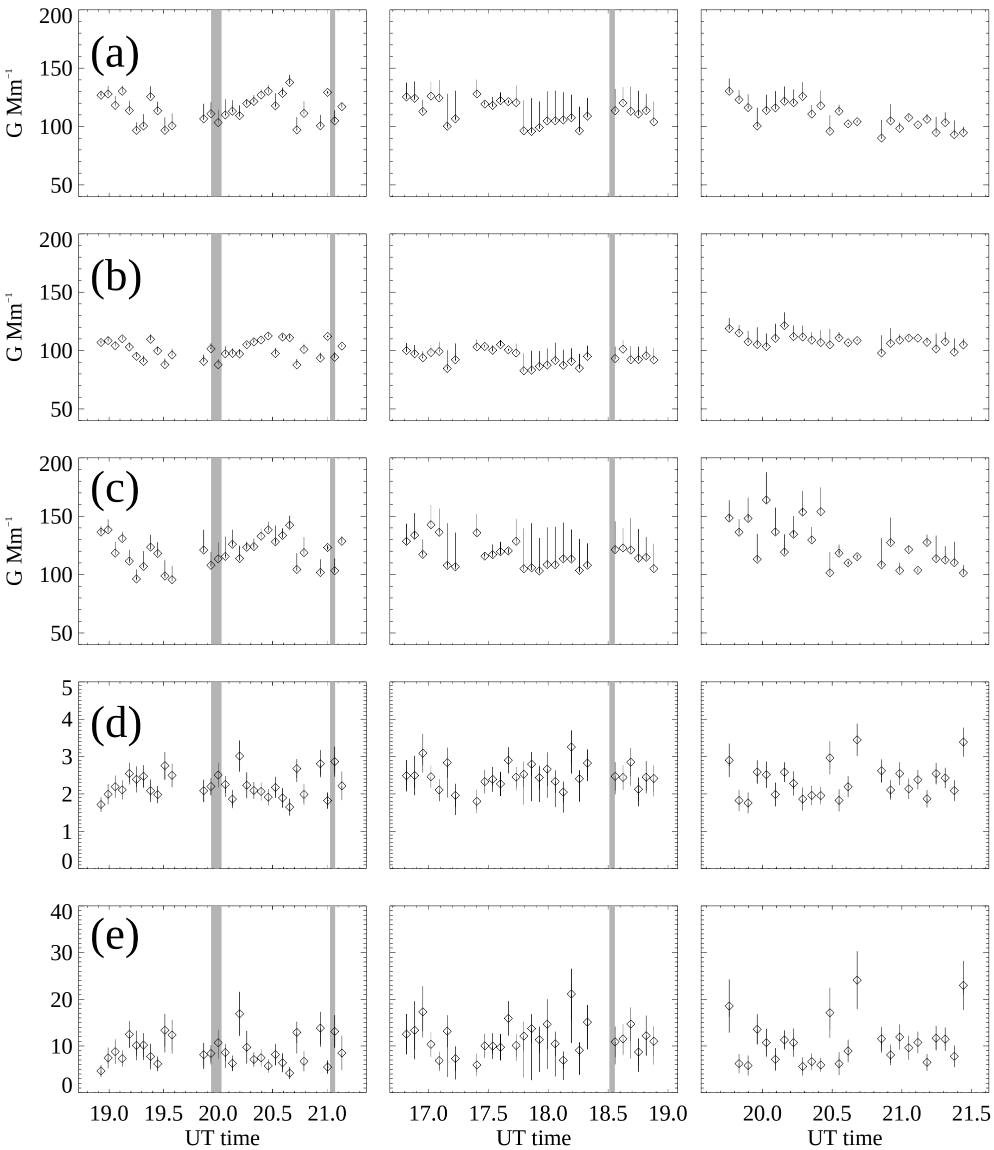

FIG. 7.—Same as Fig. 3, but for (*a*) $\overline{|\nabla_h B|}$, (*b*) $\overline{|\nabla_h B_z|}$, (*c*) $\overline{|\nabla_h B_h|}$, (*d*) $\varsigma(|\nabla_h B_h|)$, and (*e*) $\kappa(|\nabla_h B_h|)$

of 4 pixels, retaining the spatial resolution of the original data (Canfield et al. 1993; Leka & Skumanich 1999).

We consider the total current of each sign, $I^+ = \sum J_z^+ \, dA$ and $I^- = \sum J_z^- \, dA$, where J_z^+, J_z^- are the positive and negative current density, respectively, the total unsigned current $I_{\rm tot} = \sum |J_z| \, dA = I^+ + |I^-|$, and the total signed (or net) current $I_{\rm net} = \sum J_z \, dA = I^+ + I^-$, taking the absolute value of this last quantity to avoid hemispheric biases. We also consider the net current emanating from each magnetic polarity,

$$|I_{\rm net}^B| = |\sum J_z(B_z^+) \, dA| + |\sum J_z(B_z^-) \, dA| \; .$$

Under the assumption (see Wang et al. 1996 and Falconer, Moore, & Gary 2002) that all current crossing the photosphere in regions of one magnetic polarity returns to the photosphere in regions of the opposite magnetic polarity, roughly equivalent to assuming that the atmosphere above the photosphere is force-free, the region's net current can be measured using the net current emanating from either polarity. From previous studies (see, e.g., Falconer et al. 2002) it is not clear which magnetic polarity should be used, especially in cases where the active region is not fully sampled in the field of view. Hence, the quantity considered here should be comparable in magnitude to those cited in Wang et al. (1996) and Falconer et al. (2002), to within a factor of 2 but without the bias of selecting one polarity. Finally, we parameterize the distribution of $J_z(s)$ using the four moments; as outlined for changes in the vertical flux distribution (§ 3.2.1, above), current-carrying emerging flux (see Leka et al. 1996) will appear as changes in the moments of $J_z(s)$.

Examples of the parameters considered here are shown in Figure 8. There are few, if any, examples in the literature of high-cadence temporal evolution of the vertical current distributions in entire active regions as related to energetic events. Wang et al. (1994b) examined the daily variation of total vertical current in a flaring active region and hypothesize that the existence of strong current systems contribute to the flaring activity. While we find that strong currents exist in all three regions, the $I_{\rm tot}$ is actually lower in AR 8636 than in AR 0030 and in the flare-quiet AR 8891, showing

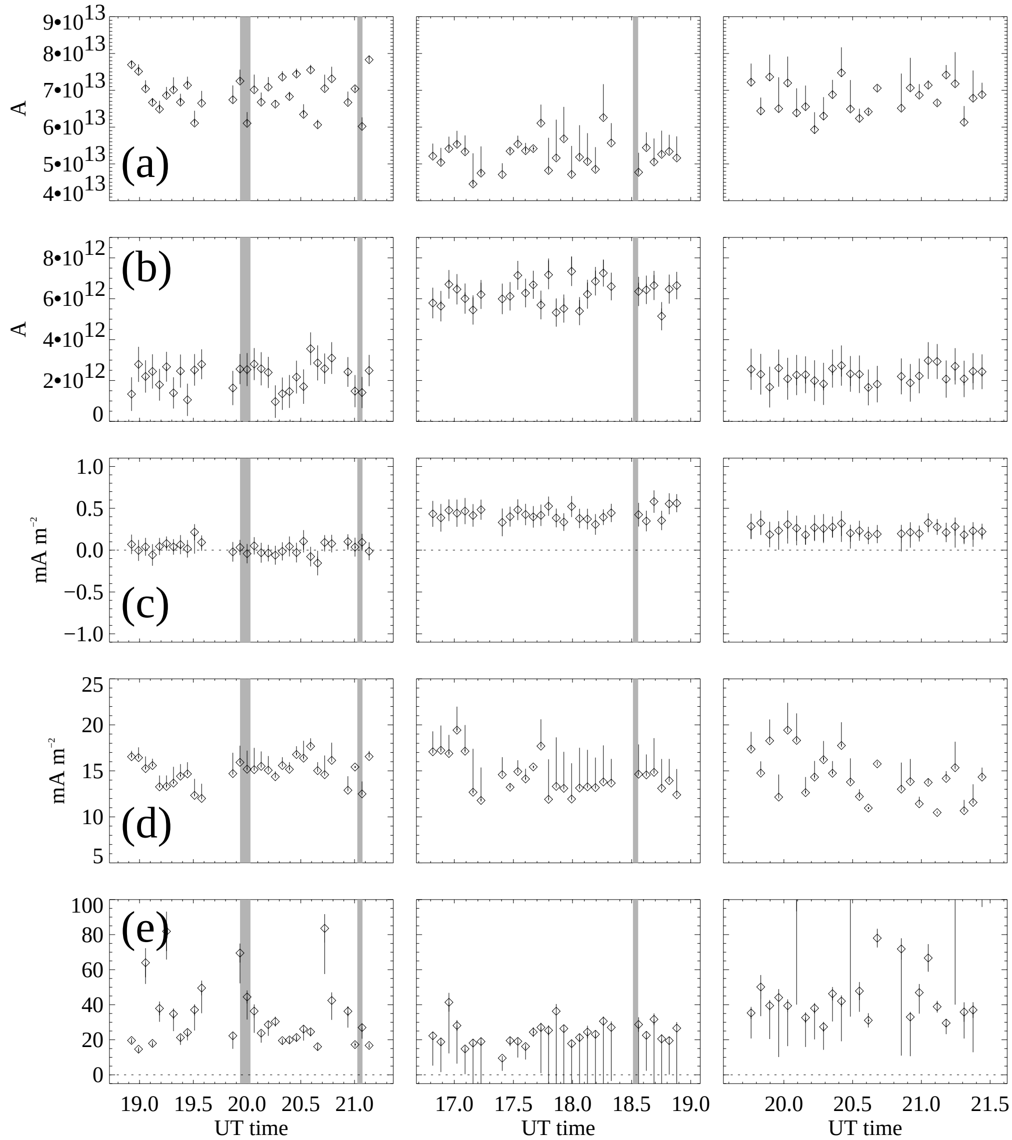

FIG. 8.—Same as Fig. 3, but for (*a*) $I_{\rm tot}$, (*b*) $|I^B_{\rm net}|$ (see Falconer et al. 2002), (*c*) $\overline{J_z}$, (*d*) $\sigma(J_z)$, and (*e*) $\kappa(J_z)$

that large $I_{\rm tot}$ is in fact not a sufficient condition for flare activity.

The $|I^B_{\rm net}|$ (Fig. 8*b*) for the three regions considered here is comparable to the magnitude of "I_N" in Falconer et al. (2002; modulo a factor of 2) for coronal mass ejection (CME)–producing active regions. We find that flare-productive AR 0030 and flare-quiet AR 8891 have similar magnitudes of $|I^B_{\rm net}|$, both smaller than that in flare-producing AR 8636. It must be noted, however, that AR 8891 did produce energetic events during its disk passage and therefore would be consistent with the Falconer et al. (2002) correlation for longer time periods.

Examining the moments of the $J_z(s)$ distribution (Fig. 8*c*–Fig. 8*e*), we find that $\overline{J_z}$ is essentially zero for AR 0030, while it is nonzero for AR 8636 and AR 8891. The $\sigma(J_z)$ is almost the same for all three regions and shows a small trend to decrease in the hour or so prior to the flare events; the variations due to seeing, however, may nullify this result for AR 8636. As has been the case before, flare-quiet AR 8891 shows decreases of similar magnitude. The $\kappa(J_z)$ parameter shows some increase prior to each of the flare events, with suitable choices for temporal windows; for AR 8891 it is widely variable but with little systematic direction. For all three regions, however, $\kappa(J_z)$ is fairly sensitive to changes in seeing.

It is evident, then, that while the distributions of $J_z(s)$ are evolving for each region, there is not an obvious preflare signature from the distribution of vertical current density.

Following Zhang (2001), we further consider the separation of the electric current density into two components:

$$\boldsymbol{J}(s) = \frac{B}{\mu_0}\nabla\times\boldsymbol{b} + \frac{1}{\mu_0}(\nabla B)\times\boldsymbol{b} \tag{8}$$

where $\boldsymbol{B} = B\boldsymbol{b}$, $\boldsymbol{b}$ being the unit vector in the direction of the field. The first term of equation (8) is dubbed the current of chirality and the second term the current of heterogeneity. By construction, the current of heterogeneity is perpendicular to the magnetic field, so whenever this term dominates over the current of chirality, the region is definitely forced. When the current of chirality dominates, the region is consistent with being force-free, although it is not definitively force-free, since the current of chirality may also have a component perpendicular to the magnetic field.

Since we do not have immediate information on the vertical gradients of the field, we are limited to the vertical components of the two terms:

$$J_z^{\rm ch}(s) = \frac{B}{\mu_0}\left(\frac{\partial b_y}{\partial x} - \frac{\partial b_x}{\partial y}\right) , \quad (9)$$

$$J_z^{h}(s) = \frac{1}{\mu_0}\left(b_y\frac{\partial B}{\partial x} - b_x\frac{\partial B}{\partial y}\right) , \quad (10)$$

where b_x and b_y are the x and y components of $\boldsymbol{b}$. On the basis of the vertical components alone, we cannot say anything definite about the forcing of the region. A vertical current of heterogeneity that is much larger than the vertical current of chirality may still be much smaller than the horizontal component of the current of chirality, so what appears in the vertical component to be a forced region may in fact be consistent with being force-free. Nevertheless, for comparison with the results of Zhang (2001), we consider the distributions of these two currents.

We show here only the most rudimentary comparisons of the bulk descriptions of these quantities (Fig. 9): the total (unsigned) currents, $I_{\rm tot}^{\rm ch}$, $I_{\rm tot}^{h}$, and the net currents, $I_{\rm net}^{\rm ch}$, $I_{\rm net}^{h}$, taking the absolute value of the latter two. Zhang (2001) examined the spatial distribution of the two and found that while there were locations in flare-productive NOAA AR 6659 where the heterogeneity term was significant, the chirality term generally dominated. In all three of our regions, the $I_{\rm tot}^{\rm ch}$ term also dominates over the $I_{\rm tot}^{h}$ term, by at least a factor of 3. If the relative magnitudes of the vertical components of these terms reflects the relative magnitudes of the full currents, then this indicates that as a whole, the regions are consistent with being force-free. These results leave open the possibility that localized parts of the active regions are forced; we leave further analysis of these intriguing quantities to a later study.

The $|I_{\rm net}^{\rm ch}|$ is nonzero for AR 8636 and AR 8891 but effectively zero in AR 0030, the most flare-productive region; $|I_{\rm net}^{h}|$ is consistent with zero for all three active regions. Such small net currents indicate general current balance over the regions, but in these examples there is no unique behavior of

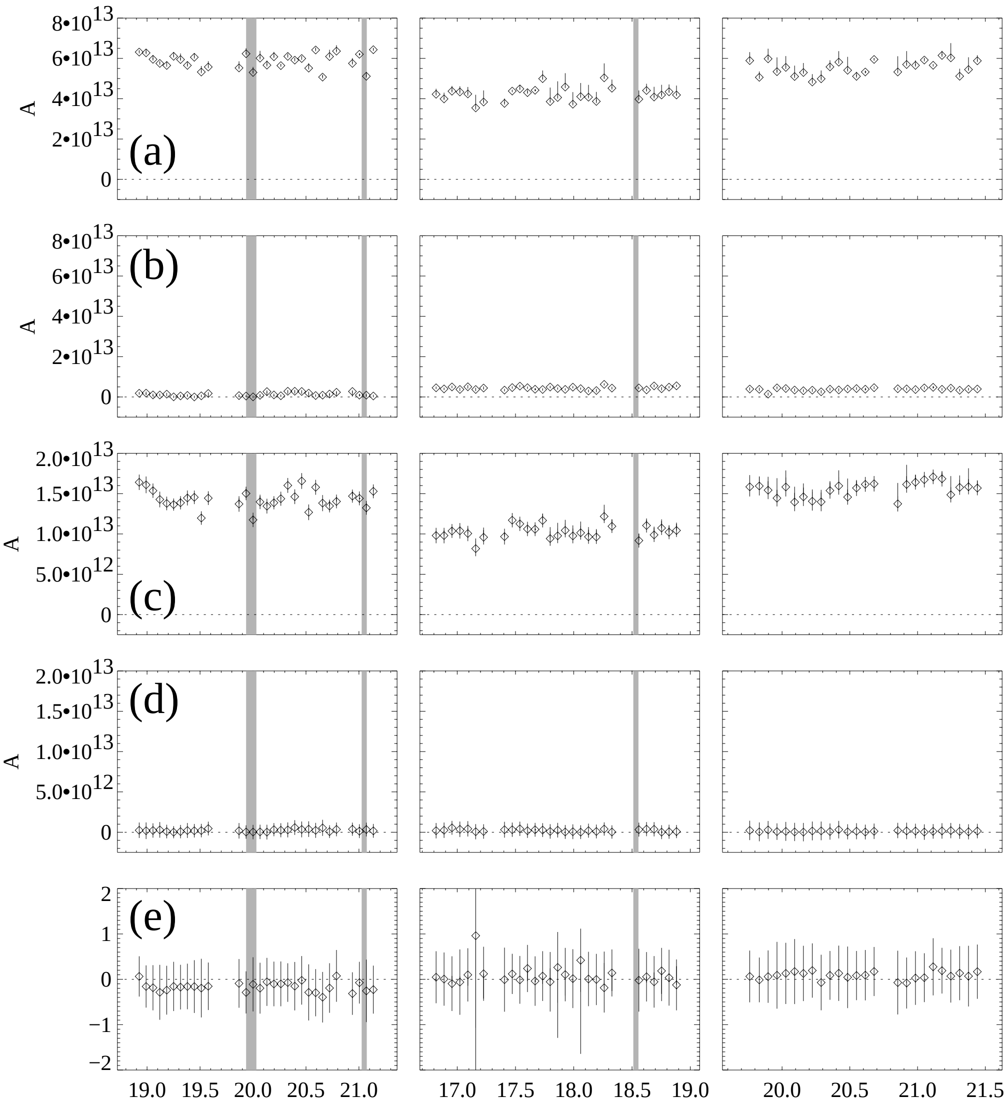

FIG. 9.—Same as Fig. 3, but for (a) $I_{\rm tot}^{\rm ch}$, (b) $|I_{\rm net}^{\rm ch}|$, (c) $I_{\rm tot}^{h}$, and (d) $|I_{\rm net}^{h}|$ (see Zhang 2001). Also plotted is (e) $\varsigma(J_z^h)$.

the net currents relative to flare productivity. There is no obvious unique flare-productivity signature in the moments of $J_z^{\rm ch}$ and J_z^h; e.g., $\varsigma(J_z^h)$ (Fig. 9) is consistent with zero over the course of the observations for all three regions. However, $\varsigma(J_z^h)$ does appear to be important when considered statistically (see Paper II).

In summary, on the hourly timescales considered for this study, we find no behavior in $|I_{\rm net}^B|$ that corresponds with the results of the days-long timescales in Falconer et al. (2002). There is no consistent flare/flare-quiet indicator in these data from $I_{\rm tot}$. There is slight evidence for a preflare rise in $\kappa(J_z)$, but no distinct preflare signature in $\overline{J_z}$ or $\sigma(J_z)$. There is evidence using the chirality/heterogeneity split for the vertical currents that these regions are, on average, consistent with being force-free; however, the evidence is equally strong that there exist localized areas within the regions that are definitely forced. No consistent result is derived using $J_z^{\rm ch}$, J_z^h, and their related spatial summations.

3.2.5. *The Twist Parameter* α

This parameter, measured in the photosphere using a variety of methods (Pevtsov, Canfield, & Metcalf 1995; Leka & Skumanich 1999; Falconer et al. 2002), is commonly referred to as the "twist" parameter for active region magnetic fields; with units of inverse length it effectively describes the pitch angle of the field's twist. In a force-free magnetic field construct, $\nabla \times \boldsymbol{B} = \alpha \boldsymbol{B}$, so that when force-freeness is assumed, α determines the full field-aligned current from the observed field vector.

The twist of active region magnetic fields has been a popular quantity to correlate with the occurrence of solar energetic events (Pevtsov et al. 1995; Falconer et al. 2002; Tian et al. 2002a). Thus far, only Pevtsov et al. (1995) has attempted to relate temporal variations in the twist of the field with flaring activity, and the relation is not clear.

We focus on two measures of α here. First, we use the ratio of the field's horizontal curl to its normal component:

$$\begin{aligned} \alpha(s) &= \frac{(\nabla_h \times \boldsymbol{B}_h)_z}{B_z} \\ &= C\frac{J_z}{B_z} \end{aligned} \tag{11}$$

(where again C represents constants relevant to MHD and unit conversions) and use the four moments of the distribution. In this formalism, J_z is inversely weighted by B_z, and thus α is preferentially sensitive to twist in regions of inclined field. As was demonstrated in Leka & Skumanich (1999) and Leka (1999), $\alpha(s)$ can vary widely over an active region. Thus, the use of the moments of $\alpha(s)$ is appropriate for a complete description of the spatial variations of the twist. Nonetheless, given its popularity in the literature, we also evaluate "$\alpha_{\rm ff}$" (referred to as "$\alpha_{\rm best}$" in Pevtsov et al. 1995), derived by minimizing the difference between a force-free field and the observed $B_h(s)$, the former computed using the observed B_z as the boundary condition. The uncertainty in $\alpha_{\rm ff}$ as shown by error bars indicate the "goodness of fit" of this single parameter to the observed morphology (see Leka & Skumanich 1999). We further take the absolute value in order to avoid hemispheric biases.

Figure 10 shows examples from both the moments of the $\alpha(s)$ distribution and $|\alpha_{\rm ff}|$. The amount of twist in the magnetic fields is larger for both AR 0030 and AR 8636 than for AR 8891, by either $\bar{\alpha}$ or by $|\alpha_{\rm ff}|$. AR 8636 approaches the 0.04 Mm^{-1} level that Tian et al. (2002a) find in the most flare-prolific regions (two additional large-α regions, AR 8210 and AR 9026, are included in Paper II); the two flaring regions considered here easily exceed the median value of 0.004 Mm^{-1} used to discriminate CME-prolific versus quiet regions in Falconer et al. (2002), while for flare-quiet AR 8891, both $\bar{\alpha}$ and $|\alpha_{\rm ff}| \approx 0$.

There is no temporal variation in either $\bar{\alpha}$ or $|\alpha_{\rm ff}|$ above the level of the uncertainties for all three regions. The appropriateness of a single "mean" or best-fit number is aptly countered here: $\sigma(\alpha)$ is similar in magnitude for all three regions and an order of magnitude larger than the means, which indicates that $\alpha(s)$ has a wide distribution both positive and negative over the active regions. The $\kappa(\alpha)$ is more variable with time (albeit with large uncertainties as well) for AR 0030, but also for AR 8891. Interestingly, the goodness-of-fit uncertainty for $|\alpha_{\rm ff}|$ is twice as large for both flaring regions than for AR 8891; hence, not only are the best-fit, or mean, α magnitudes larger for AR 0030 and AR 8636 than for AR 8891, they do worse when assuming homogeneity in the twist. In summary, there are both larger twist and *larger variation of the twist* in the flare-productive regions than in the flare-quiet region.

3.2.6. *The Current Helicity Density* h_c

The total magnetic helicity of a system in a volume V is

$$H_m = \int_V \boldsymbol{A} \cdot \boldsymbol{B} \, dV \ ,$$

where $\boldsymbol{A}$ is a vector potential for the magnetic field $\boldsymbol{B}$. In the ideal MHD approximation the total magnetic helicity is conserved, but the presence of a finite resistivity leads to the relation

$$\frac{dH_m}{dt} = -\frac{2\eta}{\mu_0} H_c \ ,$$

which relates the temporal variation of the total magnetic helicity to the total current helicity, $H_c = \int_V h_c \, dV$, $h_c = \mu_0 \boldsymbol{J} \cdot \boldsymbol{B}$ for a closed magnetic system.

In practice, a number of caveats (including the possible forced state of the photosphere and the single height sampled with these data) limit what we can immediately derive to the vertical component of the current helicity density:

$$\begin{aligned} h_c(s) &= \boldsymbol{B}_z \cdot (\nabla_h \times \boldsymbol{B}_h)_z \\ &= B_z\left(\frac{\partial B_y}{\partial x} - \frac{\partial B_x}{\partial y}\right) . \end{aligned} \tag{12}$$

In this case, J_z is directly weighted by B_z, and thus $h_c(s)$ is preferentially sensitive to twist in regions of vertical field. This quantity is determined spatially, and we therefore parameterize it with the moments of its distribution. In addition, we compute the total (unsigned) $H_c^{\rm tot} = \sum |h_c| \, dA$ and net (signed) $|H_c^{\rm net}| = |\sum h_c \, dA|$ current helicity over the active regions, the latter being akin to the current helicity imbalance described in Bao et al. (1999). These two quantities, along with the first three moments of h_c, are shown in Figure 11.

We find, interestingly, that the largest overall $H_c^{\rm tot}$ occurs in the flare-quiet AR 8891. All three regions show temporal variations in $H_c^{\rm tot}$. The net current helicity $|H_c^{\rm net}|$ is significantly different from zero for both AR 0030 and AR 8636,

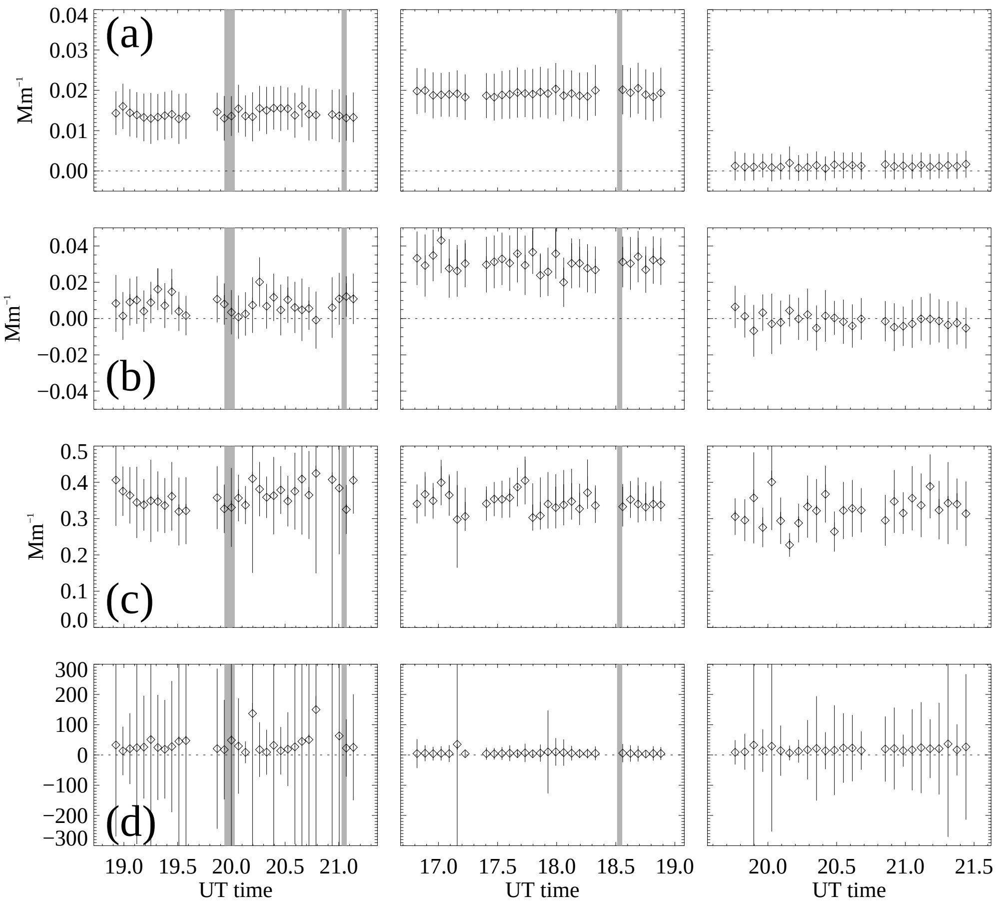

FIG. 10.—Same as Fig. 3, but for (*a*) $|\alpha_{\rm ff}|$, (*b*) $\bar{\alpha}$, (*c*) $\sigma(\alpha)$, and (*d*) $\kappa(\alpha)$

while it is consistent with zero for the entire observing period for AR 8891. This is consistent with some examples in Bao et al. (1999) for their "imbalance" parameter.

Also consistent with Bao et al. (1999), we find a larger variability in $\overline{h_c}$ for the flaring regions than in flare-quiet AR 8891, as well as a larger overall magnitude of this parameter. In addition, for both M-class flares one could argue that a decrease in $\overline{h_c}$ occurs prior to the flare (although it is not clear that such a decrease occurs prior to the X-class flare), whereas no decrease of similar magnitude occurs in AR 8891. A similar decrease in the magnitude of $\overline{h_c}$ is observed by Liu & Zhang (2002) prior to an X-class flare in localized portions of a different active region. The $\sigma(h_c)$ is, in fact, larger for AR 8891, indicating a larger range of local current helicity values present; it shows a possible preflare decrease as well. The $\varsigma(h_c)$ shows no clear flare-productivity signature.

To summarize, the current helicity density displays a number of flare-productive signatures, including a small $H_c^{\rm tot}$, nonzero $|H_c^{\rm net}|$ and $\overline{h_c}$, and a possible flare-specific decrease in $\overline{h_c}$ and $\sigma(h_c)$. Again, there is no obvious signature in $\varsigma(h_c)$, but it appears prominently when considered statistically for these and additional data and epochs (Paper II).

3.2.7. *The Shear Angles* Ψ *and* ψ

By far the most popular quantity for quantifying the degree to which an active region's observed fields deviate from that of a potential field is the "shear angle" (Hagyard et al. 1984; Hagyard, Venkatakrishnan, & Smith 1990; Ambastha et al. 1993; Wang et al. 1994a, 1994b, 1996, 2002b; Li et al. 2000b; Moon et al. 2002b; Tian, Wang, & Wu 2002b; Falconer et al. 2002). We test here many permutations of what is available using photospheric vector magnetic field data. What one strives to test is how widespread and with what magnitude the observed field is different from a potential field (derived using the observed B_z as the lower boundary condition). While restricting the analysis to the region around the primary magnetic neutral line (if such a region exists) has been popular because of the oft-observed proximity of flare emission to said neutral line, the relevant energy available for solar flares is not limited to this narrow region. Thus, we consider here both shear angles in the vicinity of the magnetic neutral line(s) [*all* magnetic neutral line(s), not only the/a primary one] and the shear angle as distributed over the entire observed active region.

Another issue is the use of the *projection* of the shear angle onto the horizontal plane (the "horizontal shear angle") versus the true angle between the observed and potential fields' respective vectors (the "three-dimensional shear angle"). A third and related issue is simply whether to use the observed transverse field or the transformed heliographic horizontal vector; we strongly advise the use of the latter, because projection effects can occur even for $\mu = \cos(\theta) = 0.95$.

Thus, we consider here the following descriptions of magnetic shear and, where appropriate, the moments of their distributions: the three-dimensional shear angle Ψ, as

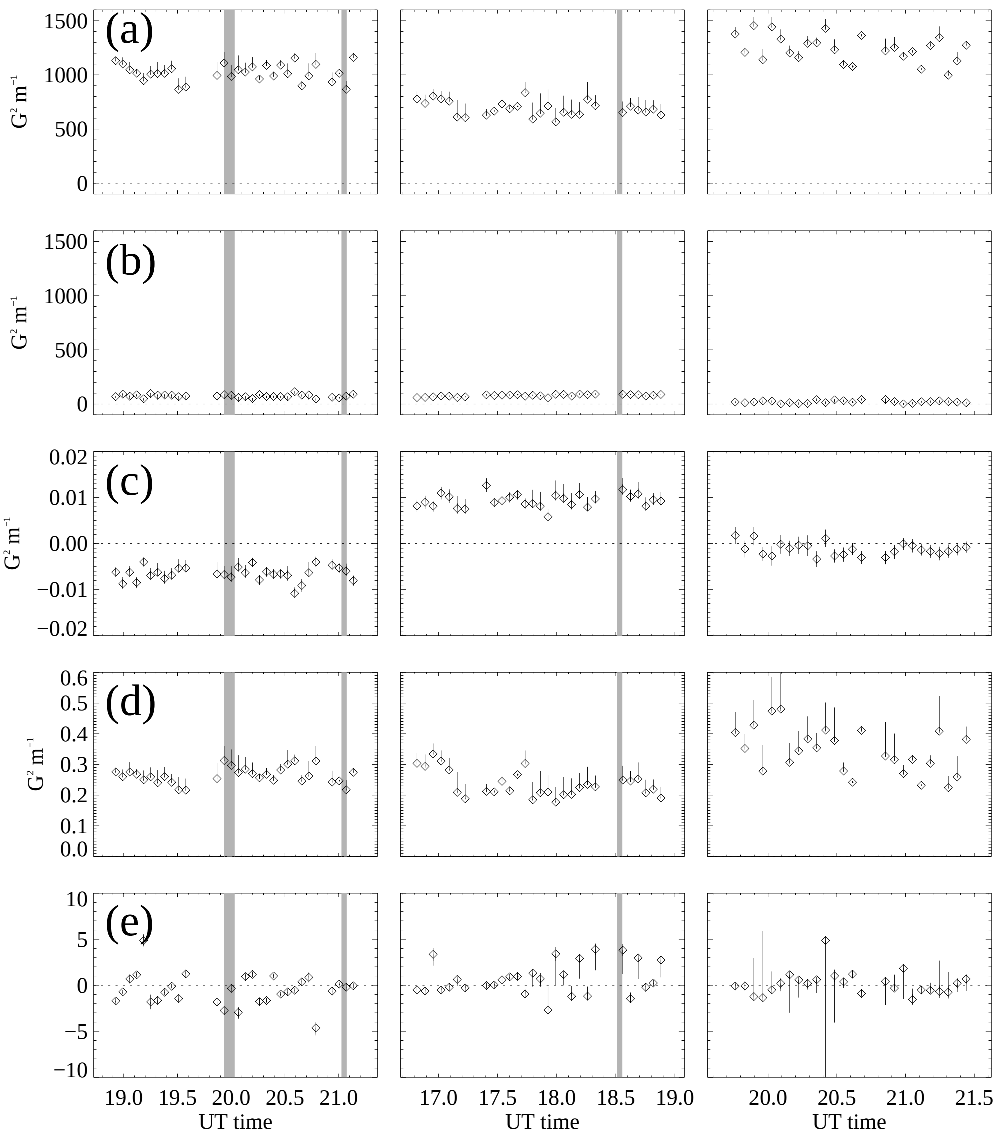

FIG. 11.—Same as Fig. 3, but for (a) $H_c^{\rm tot}$, (b) $|H_c^{\rm net}|$, (c) $\overline{h_c}$, (d) $\sigma(h_c)$, and (e) $\varsigma(h_c)$

restricted to the magnetic neutral line(s) and over the whole region and the horizontal shear angle ψ over the whole region and as restricted to the magnetic neutral line(s). Neutral-line shear angles are calculated in areas where the vertical fields are both under 500 G and transitioning between polarities, and the horizontal fields are greater than 6 σ, i.e., approximately 300 G. Both Ψ and ψ are computed using the dot product of the two relevant magnetic vectors:

$$\Psi(s) = \cos^{-1}[B^p \cdot B^o / B^p B^o] , \qquad (13)$$

$$\psi(s) = \cos^{-1}[B_h^p \cdot B_h^o / B_h^p B_h^o] , \qquad (14)$$

where superscripts o and p refer to observed and potential, respectively. The transcendental functions have large nonlinearities for small angles, i.e., where the observed field is close to potential; in these areas, a linear expansion is used when propagating the errors. In regions of large shear, however, the uncertainties are calculated from the standard propagation of errors using the uncertainties in the magnetic field components.

In addition, we calculate the number of pixels that display Ψ, $\psi > 45°$, 80°, converting these to lengths for the neutral-line shears $L(\Psi_{\rm NL} > 45°,\ 80°)$ and $L(\psi_{\rm NL} > 45°,\ 80°)$ (with the caveat that we do not require a contiguous, single neutral line and thus may include disjoint segments) and fractional areas for the whole-region calculation $A(\Psi > 45°,\ 80°)$ and $A(\psi > 45°,\ 80°)$. The goal is twofold—first, to test for flare-specific signatures using a shear angle parameterization and second, to intercompare these four shear angle–measure permutations. Since the angle range is restricted, interpreting the higher order moments of the shear angle distribution is problematic, and we limit ourselves to the first two moments.

We present first the measures of the extent of extreme magnetic shear, $A(\Psi > 80°)$, $L(\Psi_{\rm NL} > 80°)$, $A(\psi > 80°)$, and $L(\psi_{\rm NL} > 80°)$ (Fig. 12). The immediate differences between the four permutations are clear; the length of the strongly sheared neutral line(s) is greater when only the horizontal angle is computed, and the fractional area is greater, although that is due to the area restrictions placed on the definition of neutral line. In addition, the horizontal-angle

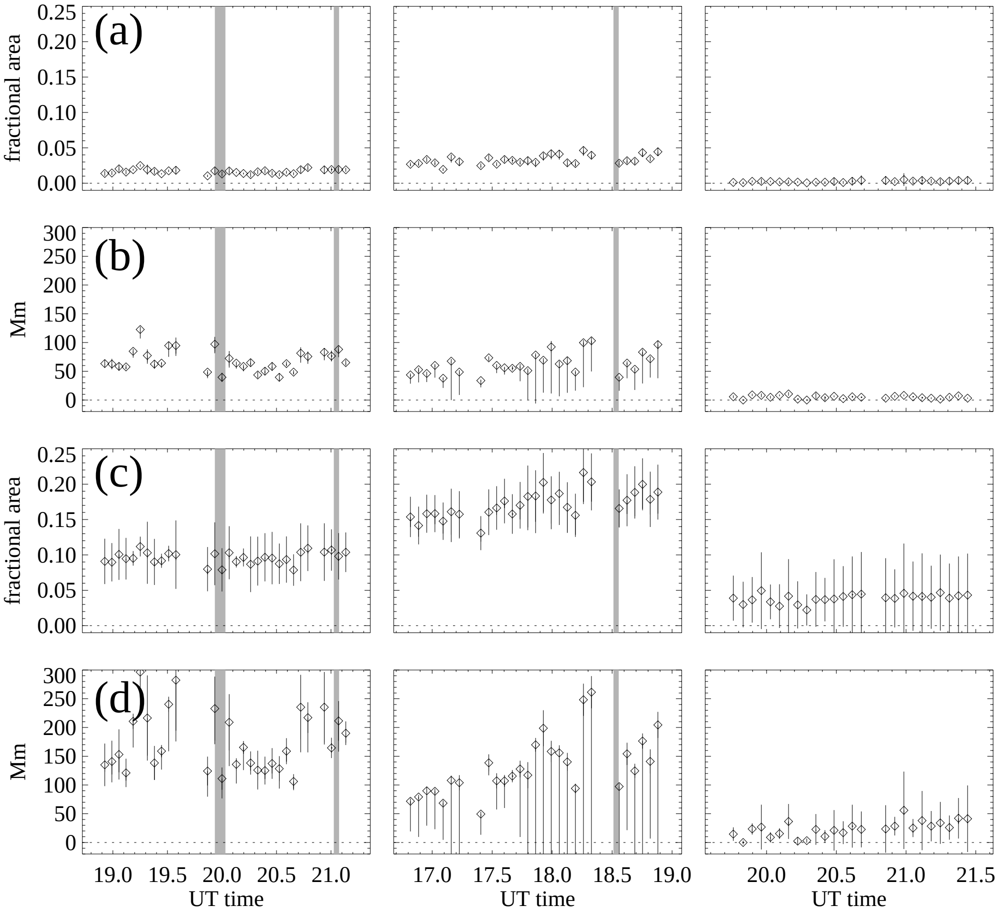

FIG. 12.—Same as Fig. 3, but for the four measures of the extent of extreme magnetic shear (*a*) $A(\Psi > 80°)$, (*b*) $L(\Psi_{NL} > 80°)$, (*c*) $A(\psi > 80°)$, and (*d*) $L(\psi_{NL} > 80°)$. As discussed in the text, those restricted to the magnetic neutral line region are given as lengths in megameters; the measures of strong shear regions are in fractional areas of the total observed active region area.

parameters have larger uncertainties and are more susceptible to seeing-induced errors than those using the full three-dimensional angle. Upon close examination, the parameters using the horizontal angle do track those using the full three-dimensional shear angle quite precisely, with essentially only a constant offset.

Concerning flare-specific indicators, for all four measures of extreme-shear extent, flare-quiet AR 8891 has a smaller measure of extreme shear than do the flare-productive regions. In addition, it displays smaller temporal variation; indeed, prior to the two M-class flares, all four measures indicate an increase in sheared fields at a level beyond that seen in AR 8891 (but also not seen prior to the X-class event in AR 0030).

As with the shear angle extent measures, we find significant differences between the moments of the shear angle distributions between the flaring regions AR 0030 and AR 8636 and the flare-quiet AR 8891 (Fig. 13). We take advantage of the continued similarity between the four permutations to present only the results from Ψ and Ψ_{NL}. The $\overline{\Psi}$ and $\sigma(\Psi)$ [and similarly $\overline{\Psi_{NL}}$, $\sigma(\Psi_{NL})$] are larger for AR 0030 and AR 8636 than for AR 8891. These results are consistent with previous studies using "daily" shear indices to correlate with flare activity (e.g., Hagyard et al. 1990; Falconer et al. 2002), with allowances for the specifics due to differing instruments and analysis: larger shear angle indices (almost independent of how they are contrived) indicate a larger probability to flare. The universality of this result is examined further in Paper II.

One might argue for a slight rise in $\overline{\Psi}$ and $\overline{\Psi_{NL}}$ prior to the flare events, consistent to some extent with Wang et al. (1994a, 2002b), Moon et al. (2002b), and some cases in Li et al. (2000b), but there is no obvious consistency with Tian et al. (2002b). The comparisons may be less obvious in some cases because we did not limit our "box" to the highly sheared regions or primary neutral lines, but rather parameterized the entire region; our inclusiveness may diminish the magnitude of the variations, but it does not incur biases or miss other subregions that are also evolving. A similar slight rise is visible in $\sigma(\Psi)$, $\sigma(\Psi_{NL})$ prior to the two M-class events but not clear prior to the X-class event; seeing effects may possibly nullify this result for AR 8636, however. These flare-prescient rises are in contrast to a steadily rising $\sigma(\Psi)$ and steadily falling $\sigma(\Psi_{NL})$ for AR 8891.

Thus, while there are numerous permutations of where to calculate and how exactly to define the magnetic shear, we find that they generally behave consistently. We find an overall agreement with previous studies that regions that have extensive shear are more immediately prone to flare events. This finding is examined further in Paper II.

3.2.8. *The Photospheric Excess Magnetic Energy Density ρ_e*

A direct measure of the energy available for energetic events is available by quantifying the total difference

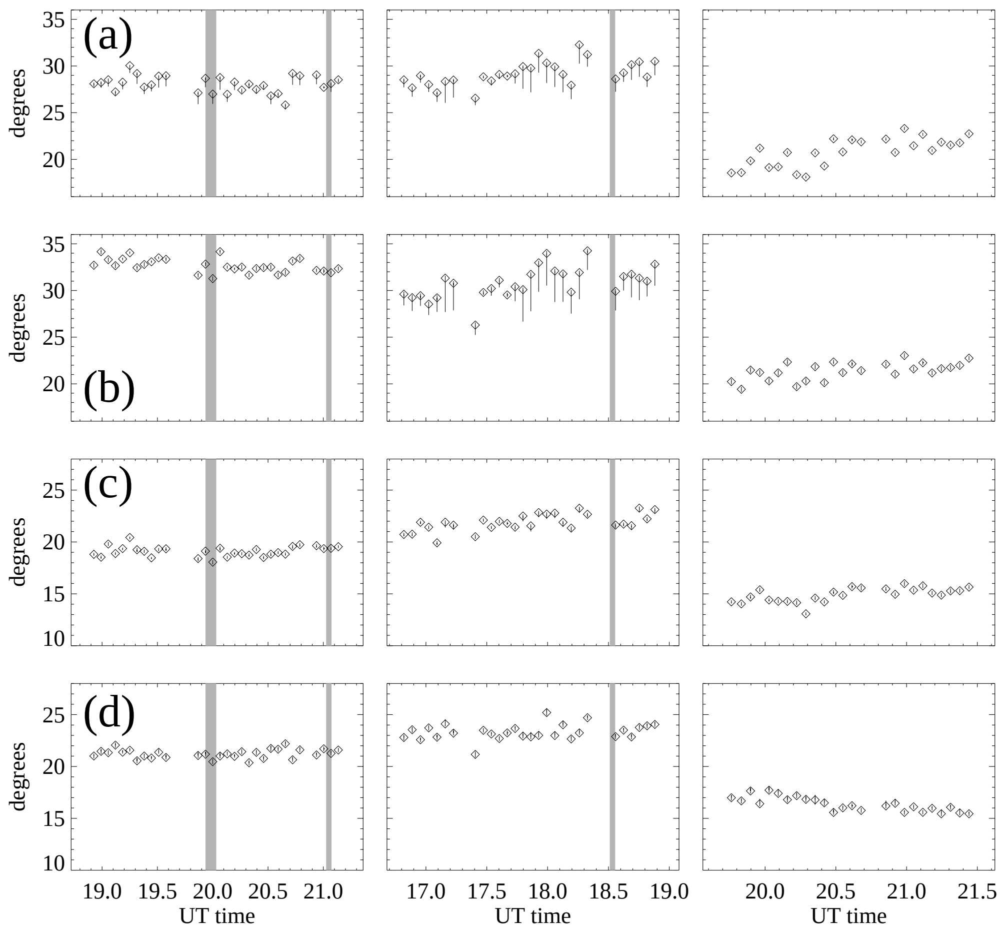

FIG. 13.—Same as Fig. 3, but for the means of the (*a*) full three-dimensional shear angles $\overline{\Psi}$, (*b*) three-dimensional shear angles around the magnetic neutral line $\overline{\Psi_{\rm NL}}$, and (*c*, *d*) the standard deviations of the same shear angles $\sigma(\Psi)$ and $\sigma(\Psi_{\rm NL})$, respectively.

between the observed and the potential fields. Using measurements in the photosphere, however, we hesitate to call this the "free energy" since the lower bound is likely forced over at least part of the active region (see discussion in § 3.2.4 of the chirality versus the heterogeneity components of the current; Metcalf et al. 1995; Moon et al. 2002a). Nonetheless, the photospheric excess magnetic energy density

$$\rho_e(s) = (B^p - B^o)^2/8\pi \tag{15}$$

(cf. Wang et al. 1996) is evaluated on a pixel-by-pixel basis, and the usual moments of the distribution are applied. In addition, the total excess energy $E_e = \sum \rho_e \, dA$ is computed over the active region; note that this is not a true total energy, since the sum effectively computes the surface, not volume, integral.

It appears once again that while both AR 0030 and AR 8636 may satisfy any energy requirement for producing a flare (with the caveat of requiring a volume integral over which we have no data), so does AR 8891. All three regions contain significant excess energy, and both the magnitudes and the temporal variations in the first two are matched in the third (Fig. 14). We find that $\overline{\rho_e}$ decreases prior to the two M-class flares but does not decrease before the X-class flare in AR 0030; it shows a decrease in flare-quiet AR 8891 as well. The $\varsigma(\rho_e)$ increases prior to flares, as does $\kappa(\rho_e)$; however, AR 8891 has similar increases and decreases, although within its larger error bars. In addition, $\varsigma(\rho_e)$ and $\kappa(\rho_e)$ are both larger for AR 8891 than for the flare-productive regions, suggesting that, counterintuitively, this flare-quiet example in fact has greater large-magnitude wings of its distribution of photospheric excess energy than do the flare-producing examples.

4. DISCUSSION

We begin here a series of investigations with the goal of extracting as much information as possible from temporally well-sampled photospheric vector magnetograph data related to the occurrence of solar energetic events. In the present manuscript, we describe in detail the data and analysis methods used, and we highlight a few parameters derivable from photospheric vector magnetograms that have been identified as related to either the energy storage required for solar energetic events or to the destabilization of the stored energy. The parameters identified have either historically been used to describe the magnetic and evolutionary state of an active region and judge its potential for future flare events or have been previously observed to vary around the time of flare events. We also highlight here a few parameters that have emerged as being potential predictors from the statistical discriminant analysis performed on the full data set in Paper II.

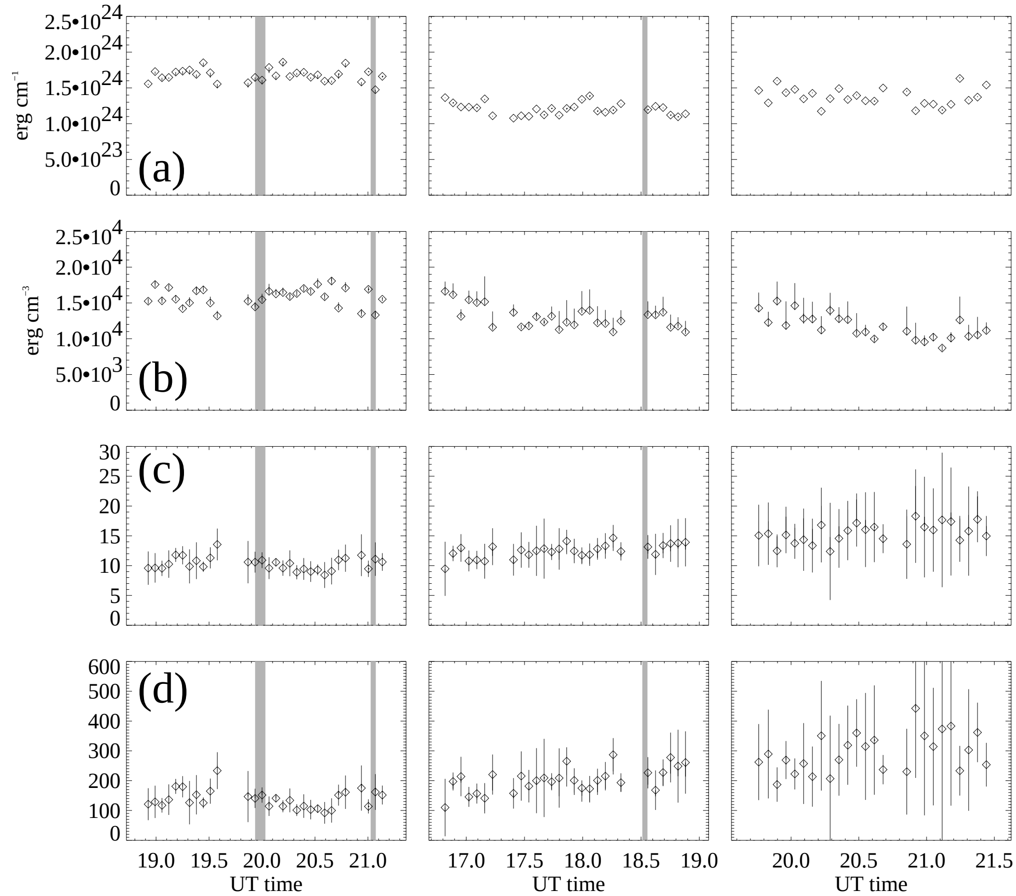

FIG. 14.—Same as Fig. 3, but for (*a*) E_e, (*b*) $\overline{\rho_e}$, (*c*) $\varsigma(\rho_e)$, and (*d*) $\kappa(\rho_e)$

This and our subsequent investigations begin with the null hypothesis, that there is no detectable signature of an impending energetic event. As such, we have selected data to specifically *not* be biased for flaring-only regions or epochs, but to include (1) flaring epochs and (2) flare-quiet epochs from the same region, even on the same day and (3) flare-quiet regions that had been given a high probability of flaring. Few studies cited here have truly examined the uniqueness of their target signature to energetic events, i.e., whether similar variations were observed during flare-quiet times (although see Bao et al. 1999). Without attempting to test the null hypothesis, it is impossible to determine whether there is a unique situation in the solar atmosphere that produces energetic events. In other words, for signature(s) to be solely related to solar energetic events, they must also *not* be present at times when no energetic event is produced.

Four issues must be reiterated here. First, we demonstrate quantitatively how changes in terrestrial atmospheric conditions can influence the results; this aspect of ground-based data has only received scant attention in prior studies. By modeling the effects of seeing on *known* data, one then quantifies the expected influence on data obtained at a different time that have known degradation in seeing quality but unknown variation due to solar evolution. One simply cannot make ad hoc assumptions about the variations of the measured quantities using data that were themselves obtained under different conditions (both solar and terrestrial). In addition, as demonstrated both here and in Leka & Rangarajan (2001), a similar blurring of the raw data can produce very different changes in the final parameterizations for different active regions and their inherently different magnetic distributions. As an example, some parameterizations are quite insensitive to seeing-induced variations (see $\Phi_{\rm tot}$, Fig. 4); some show a temporal change that may effectively be nullified if the seeing variations are accounted for [cf. AR 8636, $\overline{\nabla_h B}$, Fig. 7 and $L(\psi > 80°)$, Fig. 12], while others show temporal changes that would be exacerbated were the seeing variations in fact corrected in the data (see AR 8891 $\overline{\rho_e}$, Fig. 14).

Second, all quantities considered here are based on the physical situation at the photosphere. Observational biases and influences have been removed with the use of heliographic-plane rather than observational-plane magnetic quantities. Unsigned parameters are used where appropriate to avoid hemispheric biases. The effect of *any* limitation on the field of view of the instrument is acknowledged for the bias it can impart to, for example, the "net" quantities.

Third, by sampling the active regions both temporally and spatially and then using the moments (and where appropriate, the summations) of the resulting spatial distributions, we parameterize the magnetic state of the photosphere and quantitatively allow for uncertainties in the data and observing conditions. In this manner, we should be able to detect subtle variations caused by the evolving state of the photospheric magnetic field and avoid a "by-hand" examination of the pixel-by-pixel changes that might occur;

the latter is crucial when the data used approach statistically significant numbers.

Fourth, the photosphere may not be the appropriate region to look in the first place because of its possibly forced state and hence its physical disconnection from the chromospheric/coronal site of magnetic reconnection. There simply may not be a consistent pre-event signature to be found in the photospheric magnetic fields. To that end, a similar analysis should be performed in the future using chromospheric vector magnetic field data.

We find no obvious and consistent flare-event signatures using the parameterization of the magnetic field vector distribution and most parameters derived from the vertical current density (total, chiral, or heterogeneity terms). Similarly, inconsistent patterns are visible in higher moments of $|\nabla_h B|$ (and $|\nabla_h B_z|$, $|\nabla_h B_h|$) and in most measures deriving from the photospheric excess energy measure ρ_e.

Some parameterizations that have been tested in previous studies do not perform well here. For example, the overall magnitudes of $I_{\rm tot}$ and $|I^B_{\rm net}|$ are mixed between the flare-productive and flare-quiet regions, and the magnitudes of neither $\overline{|\nabla_h B|}$ nor $\overline{|\nabla_h B_h|}$ succeed here as a flare-probability predictor.

Counterintuitively, we find that a larger $\sigma(\gamma)$ and evolution toward a more vertical mean inclination angle is unique to a *flare-quiet* episode, as are larger $\varsigma(\rho_e)$, $\kappa(\rho_e)$, $\sigma(B_z)$, $\sigma(B_h)$, $\overline{|\nabla_h B_z|}$, and $\sigma(h_c)$ and $H_c^{\rm tot}$, as compared with the flaring epochs.

Flare-specific signatures include weak indications of increased variability, possibly a rise in $\overline{|\nabla_h B|}$ and $\overline{|\nabla_h B_z|}$, and slight evidence for a pre-event decrease in $\sigma(J_z)$ and a pre-event increase in $\kappa(J_z)$. The flare-productive regions both have a larger magnitude of the twist parameter α and are demonstrably less well represented by a single, or "best-fit," twist parameter $|\alpha_{\rm ff}|$. The current helicity density and its parameterizations show a number of unique flare-event signatures, including significant magnitudes of $|H_c^{\rm net}|$ and $\overline{h_c}$ and a greater temporal variability in the latter for the immediately flare-productive regions. The popular measure of the magnetic nonpotentiality, the magnetic shear, was indeed larger and more widespread in the flare-producing regions.

Concerning the magnetic shear angles, the four permutations examined here—i.e., using the angle between the full observed and potential field vectors or their projection onto the horizontal plane, and whether the extent of shear is considered over the entire active region or restricted to the magnetic neutral line(s)—all give similar results when examined visually. It is shown, however, that the horizontal projections have inherently greater uncertainties and are generally more susceptible to variations due to seeing than are the full vector angle difference.

In this demonstration, the variations in parameters that were observed prior to flare events were evaluated using arbitrarily selected time intervals. There was no consistency for the intervals chosen between the different parameters or even between the active regions for the same parameter. We present these results, then, as a demonstration for the need to describe a systematic, repeatable method for selecting the time interval so that results may be confirmed with subsequent observations. Such a method is explicitly outlined in Paper II.

In summary, when magnitudes and temporal variations are examined for both flare-producing and flare-quiet regions, few obvious, pre-event–specific signatures are evident. This is in agreement with the dizzying range of results in previous published studies. We expected no less, for two reasons: first, the solar atmosphere is exceedingly complicated, with no two active regions exactly alike. Second, we explicitly test the null hypothesis by including a nonflaring but similarly complicated active region for comparison to active regions in which flare events were observed. We have focused here on only three regions and as many flare events; in Leka & Barnes (2003, Paper II) we take a more quantitative approach, applying a statistical method to determine flare-specific signatures for a greater number of events and active regions.

The authors would like to thank F. A. D. for making the process of writing this paper just a little easier, and the anonymous referee for helpful comments. K. D. L. gratefully acknowledges the blood, sweat, and tears of D. L. Mickey, B. J. LaBonte, G. Nitta, and the MSO staff that went into producing the archive of IVM data. This work was carried out at the Colorado Research Associates Division of NorthWest Research Associates, Inc., with data from the University of Hawai'i Mees Solar Observatory. Funding from the Air Force Office of Scientific Research is gratefully acknowledged under contracts F49620-00-C-0004 and F49620-03-C-0019.

REFERENCES

Ambastha, A., Hagyard, M. J., & West, E. A. 1993, Sol. Phys., 148, 277
Bao, S., Zhang, H., Ai, G., & Zhang, M. 1999, A&AS, 139, 311
Canfield, R. C., Hudson, H. S., & McKenzie, D. E. 1999, Geophys. Res. Lett., 26, 627
Canfield, R. C., et al. 1993, ApJ, 411, 362
Choudhary, D. P., Ambastha, A., & Ai, G. 1998, Sol. Phys., 179, 133
Falconer, D. A., Moore, R. L., & Gary, G. A. 2002, ApJ, 569, 1016
Fontenla, J., Ambasta, A., Kalmán, B., & Csepura, G. 1995, ApJ, 440, 894
Gallagher, P., Moon, Y. J., & Wang, H. 2002, Sol. Phys., 209, 171
Giovanelli, R. G. 1939, ApJ, 89, 555
Hagyard, M. J., Smith, J. B. J., Teuber, D., & West, E. A. 1984, Sol. Phys., 91, 115
Hagyard, M. J., Venkatakrishnan, P., & Smith, J. B. J. 1990, ApJS, 73, 159
Hagyard, M. J., West, E. A., & Smith, J. B. J. 1993, Sol. Phys., 144, 141
Ishii, T. I., Kurokawa, H., & Takeuchi, T. 1998, ApJ, 499, 898
Jones, J., Bentley, R. D., Hunter, R., Iles, R. H. A., Taylor, G. C., & Thomas, D. J. 2002, poster paper presented at the 2002 NOAA Space Weather Week Conference
Krall, K. R., Smith, J. B. J., Hagyard, M. J., West, E. A., & Cummings, N. P. 1982, Sol. Phys., 79, 59
LaBonte, B. J., Mickey, D. L., & Leka, K. D. 1999, Sol. Phys., 189, 1
Landolfi, M., & Landi Degl'Innocenti, E. 1982, Sol. Phys., 78, 355
Landolfi, M., Landi Degl'Innocenti, E., & Arena, P. 1984, Sol. Phys., 93, 269
Leka, K. D. 1999, Sol. Phys., 188, 21
Leka, K. D., & Barnes, G. 2003, ApJ, 595, 1296 (Paper II)
Leka, K. D., Canfield, R. C., McClymont, A. N., & van Driel-Gesztelyi, L. 1996, ApJ, 462, 547
Leka, K. D., & Rangarajan, K. E. 2001, Sol. Phys., 203, 239
Leka, K. D., & Skumanich, A. 1999, Sol. Phys., 188, 3
Li, H., Sakurai, T., Ichimoto, K., & Ueno, S. 2000a, PASJ, 52, 465
———. 2000b, PASJ, 52, 483
Liu, Y., & Zhang, H. 2002, A&A, 386, 646
McIntosh, P. S. 1990, Sol. Phys., 125, 251
Metcalf, T. R., Litao, J., McClymont, A. N., Canfield, R. C., & Uitenbroek, H. 1995, ApJ, 439, 474
Mickey, D. L., Canfield, R., LaBonte, B. J., Leka, K. D., Waterson, M. F., & Weber, H. M. 1996, Sol. Phys., 168, 229
Moon, Y.-J., Choe, G. S., Yun, H. S., Park, Y. D., & Mickey, D. L. 2002a, ApJ, 568, 422

Moon, Y. J., Wang, H., Spirock, T. J., & Park, Y. D. 2002b, J. Korean Astron. Soc., 35, 143
Nitta, N. 1997, ApJ, 491, 402
Nitta, N., van Driel-Gesztelyi, L., Leka, K. D., & Shibata, K. 1996, Adv. Space Res., 17, 201
Patty, S. R., & Hagyard, M. J. 1986, Sol. Phys., 103, 111
Pevtsov, A. A., Canfield, R. C., & Metcalf, T. R. 1995, ApJ, 440, L109
Sawyer, C., Warwick, J. W., & Dennett, J. T. 1986, Solar Flare Prediction (Boulder: Colorado Assoc. Univ. Press)
Schmieder, B., et al. 1994, Sol. Phys., 150, 199
Silva, A., et al. 1996, ApJS, 106, 621
Tanaka, K., & Nakagawa, Y. 1973, Sol. Phys., 33, 187
Tian, L., Liu, Y., & Wang, J. 2002a, Sol. Phys., 209, 361
Tian, L., Wang, J., & Wu, D. 2002b, Sol. Phys., 209, 375
Wang, H., Ewell, M. W. J., Zirin, H., & Ai, G. 1994a, ApJ, 424, 436
Wang, H., Ji, H., Schmahl, E. J., Qiu, J., Liu, C., & Deng, N. 2002a, ApJ, 580, L177
Wang, H., Spirock, T. J., Qiu, J., Ji, H., Yurchyshyn, V., Moon, Y. J., Denker, C., & Goode, P. R. 2002b, ApJ, 576, 497
Wang, J., Shi, Z., Wang, H., & Lü, Y. 1996, ApJ, 456, 861
Wang, T., Jiong, Q., & Hongqi, Z. 1998, A&A, 336, 359
Wang, T., Xu, A., & Zhang, H. 1994b, Sol. Phys., 155, 99
Zhang, H. 2001, ApJ, 557, L71
Zhang, H., Zi, G., Yan, X., Li, W., & Liu, Y. 1994, ApJ, 423, 828
Zirin, H., & Wang, H. 1993, Sol. Phys., 144, 37